where $\mathcal{I}^{(1)}(\boldsymbol{x})-\phi_1$ is a random variable with zero mean, and $\mathcal{I}^{(1)}$ is the indicator function (2.1) for phase 1. The autocovariance $\chi(\boldsymbol{r})$ has the limiting values $\chi(0) = \phi_1\phi_2$ and $\chi(\infty) = 0$, the latter applying in the absence of long-range order. Moreover, the function $\chi(\boldsymbol{r})$ must be positive semidefinite (nonnegative) in the sense that for any finite number of spatial locations $\boldsymbol{r}_1, \boldsymbol{r}_2, \ldots, \boldsymbol{r}_m$ in $\Re^d$ and arbitrary real numbers $a_1, a_2, \ldots, a_m$,

$$\sum_{i=1}^{m}\sum_{j=1}^{m} a_i a_j \chi(\boldsymbol{r}_i - \boldsymbol{r}_j) \geq 0. \tag{2.27}$$

A variety of length scales associated with S_2 can be defined. One length scale, which we refer to as ℓ_S, is rooted in rigorous considerations:

$$\ell_S = \left\{\int_0^\infty r\chi(r)dr\right\}^{1/2} = \left\{\int_0^\infty r\left[S_2(r) - \phi_1^2\right]dr\right\}^{1/2}. \tag{2.28}$$

This length scale arises in rigorous bounds on the fluid permeability (Prager 1961) and trapping constant (Rubinstein and Torquato 1988) of three-dimensional isotropic random porous media. Since application of (2.8) for any statistically homogeneous medium leads to the result that the autocovariance of phase 1 is equal that of phase 2, i.e.,

$$\chi(\boldsymbol{r}) = S_2^{(1)}(\boldsymbol{r}) - \phi_1^2 = S_2^{(2)}(\boldsymbol{r}) - \phi_2^2, \tag{2.29}$$

it is clear that measures based on the two-point function for the phases are not capable of distinguishing length scales of phase 1 from length scales of phase 2. For example, for isotropic media, the length scale defined by (2.28) for phase 1 is identical to the corresponding one for phase 2.

Debye and Bueche (1949) showed that the two-point probability function $S_2(r)$ of an isotropic porous solid can also be obtained via scattering of radiation. Here phases 1 and 2 are the void and solid phases, respectively. The normalized scattered intensity $i(k)$ at a wave number k for a three-dimensional isotropic porous medium of volume V is proportional to the Fourier transform of the autocovariance $\chi(r)$, i.e.,

$$i(k) = 4\pi V n_o^2 \int_0^\infty \chi(r) r^2 \frac{\sin(kr)}{kr} dr, \tag{2.30}$$

where n_o is the mean density of electrons. To get the real-space two-point function $S_2(r)$ from the scattered intensity $i(k)$, one need only perform the inverse Fourier transform:

$$\chi(r) = S_2(r) - \phi_1^2 = \frac{1}{2\pi^2 V n_o^2}\int_0^\infty i(k) k^2 \frac{\sin(kr)}{kr} dk. \tag{2.31}$$

The accuracy of (2.31) depends on whether the "experimentally bandlimited" scattering curve $i(k)$ approximates sufficiently closely the entire function $i(k)$. The spectral properties of χ will be explored further below.

It has been shown (Guinier and Fournet 1955, Debye, Anderson and Brumberger 1957) that the expansion of the two-point probability function $S_2(r)$ through terms

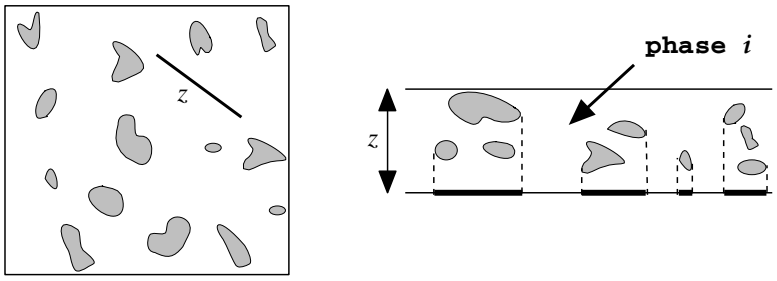

Figure 2.8 In two dimensions, the lineal-path function is the fraction of phase i obtained from a projection of a slab of thickness z onto a line.

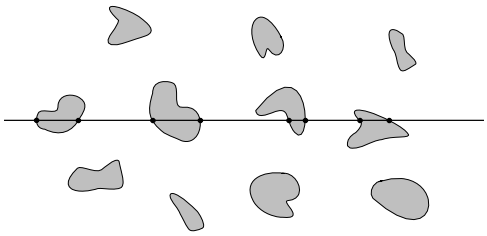

Figure 2.9 Chords are the line segments between the intersections of an infinitely long line with the two-phase interface.

Underwood (1970), "overlap" effects due to projection of the three-dimensional image and "truncation" effects due to slicing the system (see Figure 2.8).

For statistically homogeneous but anisotropic media, $L^{(i)}(\boldsymbol{z})$ will depend not only on the magnitude of vector $\boldsymbol{z}$ but on its orientation. For statistically inhomogeneous media, $L^{(i)}(\boldsymbol{x}_1, \boldsymbol{x}_2)$ will depend on the absolute positions $\boldsymbol{x}_1$ and $\boldsymbol{x}_2$ of the end points of the vector $\boldsymbol{z} = \boldsymbol{x}_2 - \boldsymbol{x}_1$.

2.5 Chord-Length Density Function

A quantity related to the lineal-path function $L^{(i)}(z)$ is the *chord-length probability density function* $p^{(i)}(z)$ (Matheron 1975, Torquato and Lu 1993). (The latter has been also called the chord-length "distribution" function.) Chords are all of the line segments between intersections of an infinitely long line with the two-phase interface (see Figure 2.9). The density function $p^{(i)}(z)$ is defined for statistically isotropic media as follows:

$$p^{(i)}(z)dz = \text{Probability of finding a chord of length between } z \text{ and } z+dz \text{ in phase } i. \tag{2.67}$$

The exclusion probabilities are related to the pair distribution functions via the expressions

$$E_V(r) = \exp\left[-\int_0^r \rho s_1(y) G_V(y) dy\right], \tag{2.101}$$

$$E_P(r) = \exp\left[-\int_0^r \rho s_1(y) G_P(y) dy\right], \tag{2.102}$$

which are obtained by use of (2.94)–(2.97). Combination of (2.94), (2.95), (2.101), and (2.102) yields

$$H_V(r) = \rho s_1(r) G_V(r) \exp\left[-\int_0^r \rho s_1(y) G_V(y) dy\right] \tag{2.103}$$

and

$$H_P(r) = \rho s_1(r) G_P(r) \exp\left[-\int_0^r \rho s_1(y) G_P(y) dy\right]. \tag{2.104}$$

We see that once any one of the triplet H_V, E_V, G_V (H_P, E_P, G_P) is known, any of the other the nearest-neighbor functions can be ascertained via the interrelations (2.92)–(2.97) and (2.101)–(2.104). The nearest-neighbor functions are *lower-order* microstructural functions, since they are lower-order cases of the canonical n-point correlation function discussed in Section 4.4

We note that there are exact conditions that the void quantities must obey when r equals the sphere radius R for any statistically homogeneous and isotropic system of identical spheres. By definitions (2.88) and (2.90), we have that

$$H_V(R) = s, \qquad E_V(R) = \phi_1, \tag{2.105}$$

where s and ϕ_1 are the specific surface and volume fraction of phase 1, respectively. This expression combined with (2.96) yields

$$G_V(R) = \frac{s}{\rho s_1(R)\phi_1}. \tag{2.106}$$

These relations are true even if the spheres overlap to varying degrees. Most of the void quantities at their extreme values are known exactly:

$$E_V(0) = G_V(0) = 1,\ H_V(0) = \rho s_1(0) \qquad E_V(\infty) = H_V(\infty) = 0.$$

Some of the particle quantities at their extreme values are known exactly:

$$E_P(0) = 1, \qquad E_P(\infty) = H_P(\infty) = 0.$$

The behavior of the functions H_P and G_P at $r = 0$ and of G_V and G_P at $r = \infty$ are microstructure-dependent (see Chapters 5 and 6).

Consider the spatial moments of H_V and H_P. The moments of H_V are trivially related to moments of the pore-size function $P(\delta)$ for the special case of spheres (see

with fixed N and V in contact with a heat bath at absolute temperature T), one has (Hansen and McDonald 1986)

$$P_N(\boldsymbol{r}^N) = \frac{e^{-\beta\Phi_N(\boldsymbol{r}^N)}}{Q_N} \qquad \text{with } Q_N = \int e^{-\beta\Phi_N(\boldsymbol{r}^N)}\, d\boldsymbol{r}^N, \tag{3.6}$$

where Q_N is the canonical *configurational partition function*, $\beta = 1/(kT)$ is a reciprocal temperature, and k is Boltzmann's constant (trivially related to the ideal gas constant). By contrast, there is an infinite number of nonequilibrium ensembles consistent with an N-particle potential.

We recall that in the context of random heterogeneous materials, our interest is in microstructures that can be taken to be independent of time. In practice, this requirement restricts us to equilibrium systems or, more generally, *quenched* nonequilibrium systems.

For time-independent ensembles consisting of *indistinguishable* particles, it is convenient to introduce the *generic* n-particle probability density function $\rho_n(\boldsymbol{r}^n)$, defined as

$$\rho_n(\boldsymbol{r}^n) = \frac{N!}{(N-n)!} \int P_N(\boldsymbol{r}^N) d\boldsymbol{r}^{N-n}, \tag{3.7}$$

where $d\boldsymbol{r}^{N-n} \equiv d\boldsymbol{r}_{n+1} d\boldsymbol{r}_{n+2} \cdots d\boldsymbol{r}_N$. In words, $\rho_n(\boldsymbol{r}^n)d\boldsymbol{r}^n$ is proportional to the probability of finding *any* subset of n particles with configuration $\boldsymbol{r}^n$ in volume element $d\boldsymbol{r}^n$. Even though it follows from (3.5) and (3.7) that ρ_n is not normalized to unity but rather

$$\int \rho_n(\boldsymbol{r}^n) d\boldsymbol{r}^n = \frac{N!}{(N-n)!}, \tag{3.8}$$

it is still commonly referred to as a "probability density function," since it can be made so trivially by dividing it by the normalization constant $N!/(N-n)!$.

For statistically homogeneous media, $\rho_n(\boldsymbol{r}^n)$ is translationally invariant and hence depends only on the relative displacements of the positions with respect to some chosen origin, say $\boldsymbol{r}_1$:

$$\rho_n(\boldsymbol{r}^n) = \rho_n(\boldsymbol{r}_{12}, \boldsymbol{r}_{13}, \ldots, \boldsymbol{r}_{1n}), \tag{3.9}$$

where $\boldsymbol{r}_{ij} = \boldsymbol{r}_j - \boldsymbol{r}_i$. In particular, the one-particle function ρ_1 is just equal to the constant *number density* of particles ρ, i.e.,

$$\rho_1(\boldsymbol{r}_1) = \rho \equiv \lim_{N,V\to\infty} \frac{N}{V}. \tag{3.10}$$

The limit indicated in (3.10) is referred to as the *thermodynamic limit*.

For statistically homogeneous media, it is convenient to define the so-called *n-particle correlation function*

$$g_n(\boldsymbol{r}^n) = \frac{\rho_n(\boldsymbol{r}^n)}{\rho^n}. \tag{3.11}$$

In systems without long-range order and in which the particles are mutually far from one another (i.e., $r_{ij} = |\boldsymbol{r}_{ij}| \to \infty$, $1 \le i < j \le N$), $\rho_n(\boldsymbol{r}^n) \to \rho^n$ and we have from (3.11)

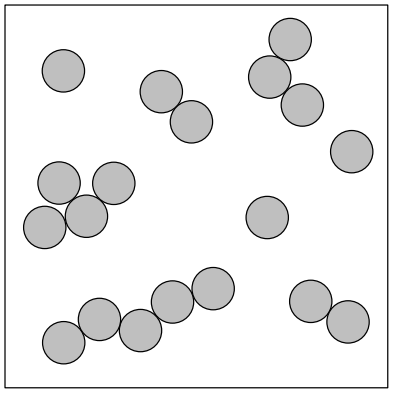

Figure 3.8 A realization of a sticky-particle system.

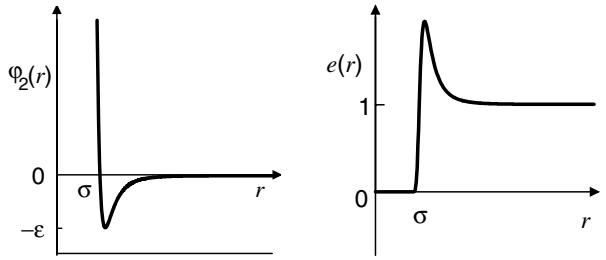

Figure 3.9 The Lennard–Jones potential (left) and the corresponding Boltzmann factor (right).

occurs in colloids. Baxter showed that this system undergoes a first-order liquid–vapor phase transition.

Lennard–Jones Potential

A well-known potential that involves both repulsive and attractive interactions and possesses a continuous first derivative is the Lennard-Jones potential (see Figure 3.9), given by

$$\varphi_2(r) = 4\epsilon\left[\left(\frac{\sigma}{r}\right)^{12} - \left(\frac{\sigma}{r}\right)^{6}\right], \tag{3.25}$$

where σ is the distance at which $\varphi_2(r) = 0$, and ϵ is the attractive well depth. The first term on the right side represents a strongly repulsive core and the second term represents a short-ranged attraction due to "dispersion" forces. The Lennard-Jones model is a prototypical potential for classical simple liquids (Hansen and McDonald 1986), such as argon, and for colloidal dispersions (Russel et al. 1989).

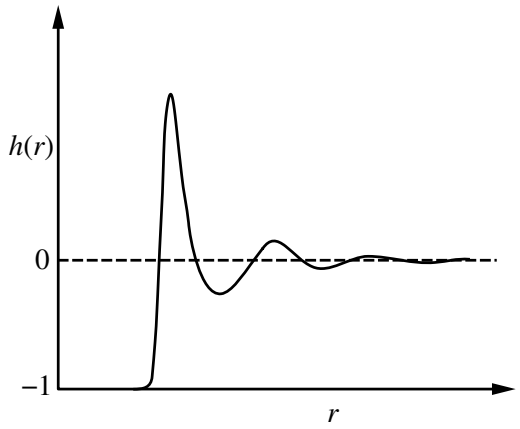

Figure 3.12 The total correlation function $h(\boldsymbol{r})$ for a typical disordered system of interacting particles.

3.2 Ornstein–Zernike Formalism

In their study of density fluctuations in fluid systems near the critical point, Ornstein and Zernike (1914) introduced the direct correlation function $c(\boldsymbol{r})$ via an integral equation that linked it to the pair correlation function $g_2(\boldsymbol{r})$. This integral equation serves as a basis for obtaining estimates of $g_2(\boldsymbol{r})$.

Consider statistically homogeneous systems of spherical particles. It is convenient to define the *total correlation function* $h(\boldsymbol{r})$ as

$$h(\boldsymbol{r}) = g_2(\boldsymbol{r}) - 1. \tag{3.30}$$

For disordered systems, $h(\boldsymbol{r})$ tends to zero when $r \to \infty$ (see Figure 3.12). In analogy with the results of Section 2.2.5, the *structure factor* $S(\boldsymbol{k})$, alluded to in Section 3.1.1, must be nonnegative, i.e., $S(\boldsymbol{k}) \equiv 1 + \rho\tilde{h}(\boldsymbol{k}) \geq 0$ for all $\boldsymbol{k}$, where $\tilde{h}(\boldsymbol{k})$ is the Fourier transform of $h(\boldsymbol{r})$. Ornstein and Zernike (1914) proposed a decomposition of h into a "direct" part and "indirect" part:

$$h(\boldsymbol{r}_{12}) = c(\boldsymbol{r}_{12}) + \rho \int h(\boldsymbol{r}_{23})c(\boldsymbol{r}_{13})d\boldsymbol{r}_3, \tag{3.31}$$

where $\boldsymbol{r}_{ij} = \boldsymbol{r}_j - \boldsymbol{r}_i$. The Ornstein–Zernike integral equation (3.31) may be considered to be a definition of the *direct correlation function* $c(\boldsymbol{r})$. We note that this definition is valid even for *nonequilibrium* systems. Note that in contrast to P_N and ρ_n defined by (3.4) and (3.7), the quantities g_2, h, and c are dimensionless.

In words, the Ornstein–Zernike equation (3.31) states that the total correlation between particles at $\boldsymbol{r}_1$ and $\boldsymbol{r}_2$ can be separated into two contributions: (i) a *direct* effect of a particle at $\boldsymbol{r}_1$ on one at $\boldsymbol{r}_2$, which is generally short-ranged (having roughly the same range as the pair potential φ_2) and is characterized by $c(\boldsymbol{r})$, and (ii) an *indirect* effect, in

Table 3.1 Some important densities for d-dimensional equilibrium hard-sphere systems.

STATE	$d = 1$	$d = 2$	$d = 3$
Freezing density, η_f	-	0.69	0.494
Maximum metastable density, η_c	-	0.83	0.644
Maximum density	1.0	$\pi/\sqrt{12} \approx 0.907$	$\pi/\sqrt{18} \approx 0.740$

singular point in the sense that it is the only point along the metastable extension with a nonzero average coordination number Z [i.e., $g_2(r)$ develops a delta-function contribution at $r = D$ as in (10.42)]. Hence, it is more accurate to refer to η_c as the MRJ state for equilibrium hard spheres.

We now describe different analytical methods to obtain the radial distribution function $g_2(r)$ for identical statistically isotropic d-dimensional hard spheres of diameter D at reduced density η in thermal equilibrium.

3.3.1 Low-Density Expansions

Before obtaining the low-density expansion of the radial distribution function $g_2(r)$, we first state an important geometrical result that will be of use to us here and in the subsequent discussions. Specifically, we note that the overlap or intersection volume $v_n^{\rm int}$ of n d-dimensional spheres of radii $a_1, a_2, \ldots, a_n$ centered at positions $\boldsymbol{x}_1, \boldsymbol{x}_2, \ldots, \boldsymbol{x}_n$ is given by the convolution integral

$$v_n^{\rm int}(\boldsymbol{x}_1, \boldsymbol{x}_2, \ldots, \boldsymbol{x}_n; a_1, \ldots, a_n) = \int d\boldsymbol{y} \prod_{i=1}^{n} \Theta(a_i - |\boldsymbol{y} - \boldsymbol{x}_i|), \tag{3.47}$$

where $\Theta(x)$ is the Heaviside step function

$$\Theta(x) = \begin{cases} 0, & x < 0, \\ 1, & x \geq 0, \end{cases} \tag{3.48}$$

and $v_1^{\rm int}(a)$ is just the volume $v_1(a)$ of a d-dimensional sphere of radius a. We denote by $v_n^{\rm int}(\boldsymbol{x}_1, \boldsymbol{x}_2, \ldots, \boldsymbol{x}_n; a)$ the intersection volume when the spheres have the same size ($a_i = a$ for all i). For example, for the first three space dimensions, the intersection volumes of two identical spheres (divided by v_1) whose centers are separated by the distance $r = |\boldsymbol{x}_2 - \boldsymbol{x}_1|$ are given by

$$\frac{v_2^{\rm int}(r; a)}{v_1(a)} = (1 - \frac{r}{2a})\Theta(2a - r), \qquad d = 1, \tag{3.49}$$

$$\frac{v_2^{\rm int}(r; a)}{v_1(a)} = \frac{2}{\pi}\left[\cos^{-1}\left(\frac{r}{2a}\right) - \frac{r}{2a}(1 - \frac{r^2}{4a^2})^{1/2}\right]\Theta(2a - r), \qquad d = 2, \tag{3.50}$$

$$\frac{v_2^{\rm int}(r; a)}{v_1(a)} = \left[1 - \frac{3}{4}\frac{r}{a} + \frac{1}{16}\left(\frac{r}{a}\right)^3\right]\Theta(2a - r), \qquad d = 3. \tag{3.51}$$

For $x \geq 1$, we introduce the function $H(\tau)$ such that

$$n(x,\tau) = \exp\Big[-(x-1)\tau\Big]H(\tau). \tag{3.69}$$

Substituting this into (3.67) yields the first-order differential equation

$$\frac{dH}{d\tau} = \frac{2e^{-\tau}}{\tau}H(\tau). \tag{3.70}$$

The initial condition $H(0) = 0$ can be determined from the previous relations by noting that $\eta(0) = 0$. Integrating (3.70) gives

$$H(\tau) = \tau^2 \exp\left[-2\int_0^\tau \frac{1-e^{-u}}{u}du\right] = \exp\big[-2(\gamma + \mathrm{Ei}(\tau))\big], \tag{3.71}$$

where $\mathrm{Ei}(\tau)$ is the exponential integral and $\gamma = 0.57721\ldots$ is Euler's constant.

For $x < 1$, the gap distribution function is given by

$$n(x,\tau) = 2\int_0^\tau du\,\frac{H(u)}{u}e^{-xu}. \tag{3.72}$$

The density of adsorbed rods is calculated from (3.66) by substituting the expression for $n(x,\tau)$ in (3.72) and integrating with respect to x:

$$\eta(\tau) = \int_0^\tau du\,\frac{H(u)}{u^2}. \tag{3.73}$$

At the saturation limit (i.e., as $\tau \to \infty$), the maximum density is exactly

$$\eta_c = \eta(\tau = \infty) = \int_0^\infty du\,\frac{H(u)}{u^2} \approx 0.7476. \tag{3.74}$$

Moreover, we can expand the reduced density of (3.73) about $\tau^{-1} = 0$ to give

$$\eta(\tau) \sim \eta(\infty) - \frac{\exp(-2\gamma)}{\tau},$$

and hence for large τ we have the asymptotic algebraic behavior

$$\eta(\infty) - \eta(\tau) \sim \tau^{-1}. \tag{3.75}$$

Evaluating the gap distribution function (3.72) at the final state $\tau = \infty$ shows that it diverges logarithmically as $x \to 0$, implying the same logarithmic singularity in the pair correlation function $g_2(x+1,\infty)$, i.e.,

$$g_2(x+1,\infty) = -2[\eta(\infty)]^{-2}\exp(-2\gamma)\ln x, \quad x \to 0. \tag{3.76}$$

Indeed, an analytical integral expression for the pair correlation function $g_2(x+1,\tau)$ at any τ or density has been given recently by Bonnier et al. (1994) that at the saturation limit exhibits the expected logarithmic divergence. Calculation of the integral relation for g_2 becomes progressively difficult as x increases from zero. However, owing to the fact that the g_2 decays to its long-range value very rapidly after $x \approx 2$ (even at the saturation limit), one need not evaluate the expression for large distances.

Bonnier et al. (1994) also showed that the pair correlation function has *super-exponential* decay. Specifically, they found that at any finite time τ or density η,

$$g_2(x+1,\eta) \sim \frac{1}{\Gamma(x+1)}\left(\frac{2}{\ln x}\right)^x, \quad x \to \infty. \tag{3.77}$$

Thus, g_2 is a short-ranged function at any density. This turns out to be true in higher dimensions as well.

It can be shown that the aforementioned exclusion probability $E_V(x,\tau)$ for $x \geq 1$ at time τ is given by (Rintoul, Torquato and Tarjus 1996)

$$E_V(x,\tau) = \frac{H(\tau)}{\tau^2} e^{-2(x-1)\tau}, \quad x \geq 1. \tag{3.78}$$

Hence, according to (3.65), the fraction of available space when a test particle of unit length is added to the system at some fixed time is given by

$$E_V(1,\tau) = \frac{H(\tau)}{\tau^2}. \tag{3.79}$$

Since small times imply small densities, we can manipulate the expansions of (3.71) and (3.73) in powers of τ to give the small-density expansion of the fraction of available space as

$$E_V(1,\eta) = 1 - 2\eta + \frac{1}{2}\eta^2 + \frac{2}{9}\eta^3 + \mathcal{O}(\eta^4). \tag{3.80}$$

This last expansion is to be compared with the corresponding expansion of the exact expression $E_V(1,\eta) = (1-\eta)\exp[-2\eta/(1-\eta)]$ for an equilibrium system of hard rods (Section 5.2.5), which expands as

$$E_V(1,\eta) = 1 - 2\eta + \frac{1}{2}\eta^2 + \frac{1}{3}\eta^3 + \mathcal{O}(\eta^4). \tag{3.81}$$

We see that the RSA and equilibrium expansions are the same up through order η^2 but differ at third- and higher-order terms, behavior consistent with the opening remarks of this section.

3.4.2 Identical Hard Spheres in Higher Dimensions

In contrast to the one-dimensional instance, there are no analytical solutions for the coverage at the saturation limit for identical d-dimensional hard spheres for $d \geq 2$. Consequently, RSA processes at high densities for $d \geq 2$ have been primarily investigated using computer simulation techniques. Numerical experiments have yielded that $\eta(\infty) \approx 0.547$ for $d = 2$ (hard disks) (Feder 1980) and $\eta(\infty) \approx 0.38$ for $d = 3$ (hard spheres) (Cooper 1988) in the thermodynamic limit.

In his numerical study of RSA hard disks, Feder (1980) postulated that the asymptotic coverage for d-dimensional hard spheres follows the algebraic behavior

$$\eta(\infty) - \eta(\tau) \sim \tau^{-1/d}. \tag{3.82}$$

by (Steinhardt, Nelson and Ronchetti 1983)

$$Q_6 \equiv \left(\frac{4\pi}{13} \sum_{m=-6}^{6} \left| \overline{Y_{6m}} \right|^2 \right)^{1/2}, \tag{3.85}$$

where $\overline{Y_{6m}}$ denotes an average over all bonds. For a completely disordered system in the infinite-volume limit, Q_6 equals zero, whereas Q_6 attains its maximum value for space-filling jammed structures ($Q_6^{\mathrm{FCC}} \approx 0.575$) in the perfect FCC crystal. Thus, Q_6 provides a global measure of FCC crystallite formation in the system. For convenience, we normalize the orientational order metric by its value in the perfect FCC crystal, i.e., $Q \equiv Q_6/Q_6^{\mathrm{FCC}}$.

Scalar measures of translational order have not been well studied. Torquato et al. (2000) have introduced a simple translational order metric T that measures the degree of spatial ordering, relative to the perfect FCC lattice at the same volume fraction. Specifically,

$$T = \left| \frac{\sum_{i=1}^{N_C} (n_i - n_i^{\mathrm{ideal}})}{\sum_{i=1}^{N_C} (n_i^{\mathrm{FCC}} - n_i^{\mathrm{ideal}})} \right|, \tag{3.86}$$

where n_i, for the system of interest, denotes the average occupation number for the shell of width $a\delta$ centered at a distance from a reference sphere that equals the ith nearest-neighbor separation for the open FCC lattice at that density. Moreover, a is the first nearest-neighbor distance for that FCC lattice, and N_C is the total number of shells. Similarly, n_i^{ideal} and n_i^{FCC} are the corresponding shell occupation numbers for an ideal gas (spatially uncorrelated spheres) and the open FCC lattice. Observe that $T = 0$ for an ideal gas (perfect randomness), and $T = 1$ for perfect FCC spatial ordering.

Both Q and T are crystal-dependent measures in that they measure order with respect to the FCC lattice. Other reasonable choices for order metrics have been tested, including crystal-independent ones, such as an information-theoretic *entropy*, another translational-order metric, and a "local" version of Q. Importantly, the evaluations of these order metrics resulted in the same qualitative behavior as that given by Q and T for the configurations discussed immediately below. All of these results, as well as the utility of other, more sophisticated, order metrics for many-particle systems in general, are described by Truskett, Torquato and Debenedetti (2000) and Kansal, Truskett and Torquato (2000a).

3.5.4 Molecular Dynamics Simulations

To support the aforementioned arguments, Torquato et al. (2000) carried out molecular dynamics simulations (Chapter 12) using systems of 500 identical hard spheres with periodic boundary conditions. Starting from an equilibrium liquid configuration at a volume fraction $\eta = 0.3$, the system was compressed to a jammed state by the well-known method of Lubachevsky and Stillinger (1990), which allows the diameter of the particles to grow linearly in time with a dimensionless rate Γ. The jammed state

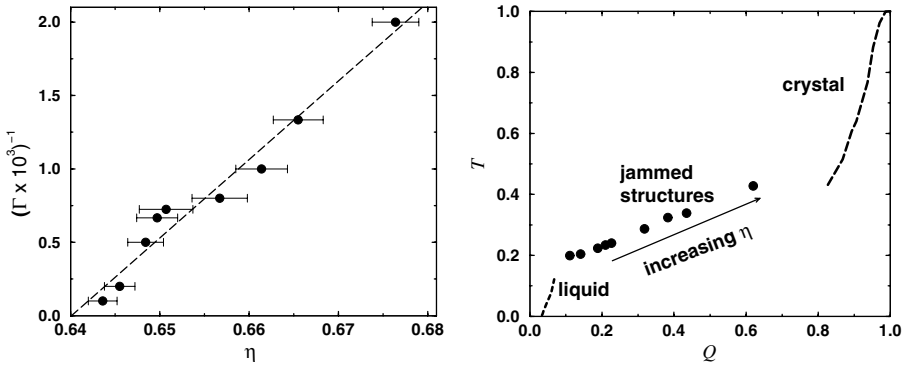

Figure 3.18 Left panel: The reciprocal compression rate Γ^{-1} versus the volume fraction η of the final jammed state of hard spheres obtained using the molecular dynamics compression protocol of Lubachevsky and Stillinger (1990). Right panel: The Q-T plane for the hard-sphere system, where T and Q are translational and orientational order metrics, respectively (where $\delta = 0.196$ and $N_C = 7$). Shown are the average values for the jammed states, as well as states along the equilibrium liquid (dotted) and crystal (dashed) branches.

occurs when the diameters can no longer increase in time, the sphere collision rate diverges, and no further compression can be achieved after relaxing the configuration at the jammed volume fraction. Figure 3.18 shows that the volume fraction of the final jammed states is inversely proportional to the compression rate Γ. A linear extrapolation of the data to the infinite compression rate limit yields $\eta \approx 0.64$, which is close to the supposed RCP value reported by Scott and Kilgour (1969). Figure 3.19 shows a jammed configuration at $\eta \approx 0.64$.

The relationship between translational and bond-orientational ordering was characterized for the first time by Torquato et al. (2000). Figure 3.18 shows their results for the aforementioned jammed structures in the Q-T plane. This order plot reveals several key points. First, T and Q are positively correlated and therefore are essentially equivalent measures of order for the jammed structures. Second, they found that the MRJ packing fraction η_M is approximately equal to 0.64 for 500-sphere systems using the Lubachevsky–Stillinger protocol. It should be noted, however, that a systematic study of other protocols may indeed find jammed states with a lower degree of order as measured by Q or some other order metric. Lastly and most importantly, the degree of order increases monotonically with the jammed packing fraction. These results demonstrate that the notion of RCP as the highest possible density that a random sphere packing can attain is ill-defined, since one can achieve packings with arbitrarily small increases in volume fraction at the expense of small increases in order.

For purposes of comparison, the order plot of Figure 3.18 includes results for the equilibrium hard-sphere system for densities along the stable liquid branch and stable crystal branch (ending at the maximum close-packed FCC state). Interestingly, the equilibrium structures exhibit the same monotonicity properties as the jammed struc-

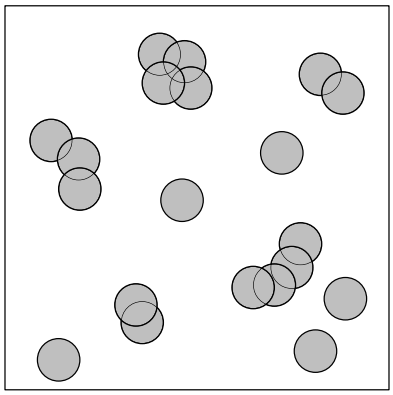

Figure 4.1 Portion of a realization of possibly overlapping two-dimensional spheres (i.e., circular disks). Phase 1 is the space $\mathcal{V}_1$ exterior to the particles (unshaded region). Phase 2 is the space $\mathcal{V}_2$ occupied by the particles (shaded region).

$\mathcal{I}(\boldsymbol{x})$ for the matrix phase is given by

$$\begin{aligned}\mathcal{I}(\boldsymbol{x};\boldsymbol{r}^N) &= \prod_{i=1}^{N}\left[1-m(|\boldsymbol{x}-\boldsymbol{r}_i|;R)\right]\\ &= 1-\sum_{i=1}^{N} m(|\boldsymbol{x}-\boldsymbol{r}_i|;R)+\sum_{i<j}^{N} m(|\boldsymbol{x}-\boldsymbol{r}_i|;R)m(|\boldsymbol{x}-\boldsymbol{r}_j|;R)\\ &\quad -\sum_{i<j<k}^{N} m(|\boldsymbol{x}-\boldsymbol{r}_i|;R)m(|\boldsymbol{x}-\boldsymbol{r}_j|;R)m(|\boldsymbol{x}-\boldsymbol{r}_k|;R)+\cdots,\end{aligned} \tag{4.3}$$

where the *exclusion-region* indicator function $m(r;R)$ is defined by

$$m(r;R)=\Theta(R-r)=\begin{cases}1, & r\le R,\\ 0, & r>R,\end{cases} \tag{4.4}$$

and $\Theta(x)$ is the Heaviside step function (3.48). The volume *excluded* to the center of a spherical inclusion of radius R by a point "test" particle is itself a spherical region of radius R. This is why we refer to $m(r;R)$ as an exclusion-region indicator function. Importantly, if the test particle had nonzero size, then the exclusion region would not simply be a spherical region of radius R (see Figure 4.3). Note that the kth sum in (4.3) is over all distinguishable k-tuplets of possibly overlapping particles and thus contains $N!/[(N-k)!k!]$ terms. The first sum accounts for regions of space occupied by N spheres (without any overlap); the second sum accounts for possible overlap between pairs of spheres; the third sum accounts for possible overlap between triplets of spheres, etc.

For statistically *inhomogeneous* media, we can explicitly find an expression for $S_1(\boldsymbol{x})$ by ensemble averaging (4.3), i.e.,

$$s \leq \int \delta(R - r_{12})\rho_1(\boldsymbol{r}_2)d\boldsymbol{r}_2 - \int \delta(R - r_{12})m(r_{13})\rho_2(\boldsymbol{r}_{23})d\boldsymbol{r}_2 d\boldsymbol{r}_3 + \frac{1}{2}\int \delta(R - r_{12})m(r_{13})m(r_{14})\rho_3(\boldsymbol{r}_{23}, \boldsymbol{r}_{24})d\boldsymbol{r}_2 d\boldsymbol{r}_3 d\boldsymbol{r}_4,$$

which are the first three partial sums of (4.9) using the aforementioned change of variables. More generally, if $w^{(\ell)}$ denotes the partial sum of the series (4.9) from $k = 1$ up to $k = \ell$, then we have

$$s \left\{ \begin{matrix} \geq \\ \leq \end{matrix} \right\} \begin{cases} w^{(\ell)} & \text{for } \ell \text{ even}, \\ & \text{for } \ell \text{ odd}. \end{cases} \tag{4.15}$$

4.1.2 Example Calculations

It is instructive to describe how one evaluates the one-point expressions (4.5) and (4.9) for S_1 and s for some statistically homogeneous model microstructures given the n-particle functions ρ_n. Calculations of higher-order correlation functions are given in the next several chapters.

Consider homogeneous ensembles of d-dimensional identical spheres of radius R at number density ρ. Recall from Chapter 3 that the dimensionless, or *reduced*, density η is defined by

$$\eta = \rho \upsilon_1(R), \tag{4.16}$$

where $\upsilon_1(R)$ is d-dimensional volume of a *single* sphere is given by

$$\upsilon_1(R) = \frac{\pi^{d/2}}{\Gamma(1 + d/2)} R^d, \tag{4.17}$$

and $\Gamma(x)$ is the gamma function. For example, for $d = 1, 2$, and 3, $\upsilon_1(R) = 2R$, πR^2, and $4\pi R^3/3$, respectively. The corresponding d-dimensional surface area of a *single* sphere, denoted by $s_1(R)$, is just

$$s_1(R) = \frac{\partial \upsilon_1}{\partial R} = \frac{d\pi^{d/2}}{\Gamma(1 + d/2)} R^{d-1}. \tag{4.18}$$

For $d = 1, 2$, and 3 this yields $s_1(R) = 2$, $2\pi R$, and $4\pi R^2$, respectively.

First, we evaluate relations (4.5) and (4.9) for the extreme limits of the cherry-pit model [cf. (3.27) and Figure 3.10], i.e., $\lambda = 0$ (fully penetrable spheres) and $\lambda = 1$ (totally impenetrable spheres). Then we discuss calculations for arbitrary values of the impenetrability parameter λ.

Fully Penetrable Spheres, $\lambda = 0$

For homogeneous fully penetrable spheres, we recall that ρ_n is trivially equal to the constant ρ^n [cf. (3.18)]. Substitution of this relation into (4.5) with $S_1 = \phi_1$ yields

$$\phi_1(R) = 1 + \sum_{k=1}^{\infty} \frac{(-\rho)^k}{k!} \int \prod_{j=1}^{k} m(|\boldsymbol{x} - \boldsymbol{r}_j|; R)d\boldsymbol{r}_j = 1 + \sum_{k=1}^{\infty} \frac{(-\rho)^k}{k!} \upsilon_1^k(R),$$

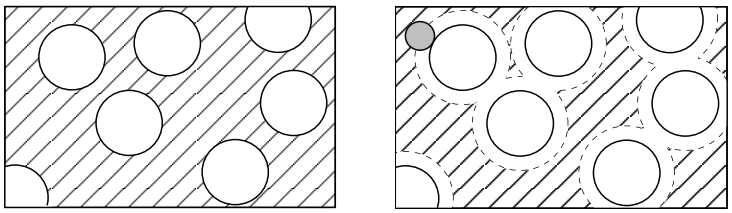

Figure 4.3 The same system of identical spheres of radius R is shown in both panels. However, the available spaces (cross-hatched regions) to a point test particle (left panel) and a nonzero-sized test particle (right panel) are clearly different. Here b and $a = b + R$ are the radii of the test particle and exclusion sphere, respectively.

is the *exclusion sphere indicator function*. Similarly, we have that the indicator function for the available surface $\mathcal{S}_i$ is given by

$$\begin{aligned}\mathcal{M}(\boldsymbol{x}; a_i) &= -\frac{\partial \mathcal{I}(\boldsymbol{x}; a_i)}{\partial a_i} \\ &= \sum_{j=1}^{N} \delta(|\boldsymbol{x} - \boldsymbol{r}_j| - a_i) - \sum_{j<k}^{N} \delta(|\boldsymbol{x} - \boldsymbol{r}_j| - a_i) m(|\boldsymbol{x} - \boldsymbol{r}_k|; a_i) \\ &\quad - \sum_{j<k}^{N} \delta(|\boldsymbol{x} - \boldsymbol{r}_k| - a_i) m(|\boldsymbol{x} - \boldsymbol{r}_j|; a_i) + \cdots, \end{aligned} \tag{4.31}$$

where $\delta(\boldsymbol{x})$ is the Dirac delta function. Clearly, $\mathcal{M}(\boldsymbol{x}; a_i)$ is a function that is zero everywhere except when $\boldsymbol{x}$ describes a position on $\mathcal{S}_i$. Equations (4.29) and (4.31) generalize the corresponding relations derived by Torquato and Stell (1982), and by Torquato and Stell (1984) and Chiew and Glandt (1984), respectively, for the special case in which all $b_i = 0$ and all $a_i = R$.

The ensemble averages of $\mathcal{I}(\boldsymbol{x}; a_i)$ and $\mathcal{M}(\boldsymbol{x}; a_i)$ are simply the volume fraction $S_1(\boldsymbol{x}; a_i) = \phi_1(\boldsymbol{x}; a_i)$ and specific surface $s(\boldsymbol{x}; a_i)$ associated with the available space D_i and the available surface $\mathcal{S}_i$, respectively. It is only when all $b_i = 0$ and all $a_i = R$ that these two averages are, respectively, equal to the usual position-dependent matrix volume fraction $S_1(\boldsymbol{x}; R) = \phi_1(\boldsymbol{x}; R)$ and the specific surface of the particle–matrix interface $s(\boldsymbol{x}; R)$.

We now define a more general n-point function G_n in terms of available-space indicator functions for the case of a mixture of n test particles of radii $b_1, \ldots, b_n$ at positions $\boldsymbol{x}^n \equiv \{\boldsymbol{x}_1, \boldsymbol{x}_2, \ldots, \boldsymbol{x}_n\}$, and N identical spherical inclusions of radius R:

of two and three circles. An analytical expression for the intersection area of three circles was given by Rowlinson (1964). For $d = 3$, Kratky (1981) also showed that the intersection volumes of five or more spheres of equal radius can be expressed as a linear combination of intersection volumes of two, three, and four spheres. The intersection volumes of three spheres (Powell 1964) and four spheres (Helte 1994) are known analytically. Therefore, in principle, the exact intersection (and hence union) area of n disks or volume of n spheres of equal radius can be exactly computed.

5.1.1 n-Point Probability Functions

The n-point probability function S_n for phase 1 (matrix phase) is obtained from the general definition (4.69) in terms of the canonical function, i.e, $S_n(\boldsymbol{x}^n) = H_n(\emptyset; \boldsymbol{x}^n; \emptyset)$ in the limit that all of the radii of the test particles shrink to zero (or $a_i \to R, \forall i$). This definition and expression (5.1) yield the exact relation

$$S_n(\boldsymbol{x}^n) = \exp\Big[- \rho v_n(\boldsymbol{x}^n; R)\Big] \tag{5.6}$$

for d-dimensional fully penetrable spheres, where $v_n(\boldsymbol{x}^n; R)$ denotes the union volume of n identical spheres of radius R. The general expression (5.6) was derived first by Torquato and Stell (1983b), who referred to S_n as the n-point *matrix* probability functions.

When $n = 1$, we see that this expression gives

$$S_1 = \phi_1 = \exp(-\eta),$$

which is in agreement with relation (4.19) for the "matrix" volume fraction ϕ_1 given earlier. Recall that $\eta = \rho v_1(R)$ is a reduced density [cf. (4.16)], where $v_1(R)$ is given by (4.17) in d dimensions.

When $n = 2$, we see that relation (5.6) gives

$$S_2(r) = \exp\Big[- \eta \frac{v_2(r; R)}{v_1(R)}\Big], \tag{5.7}$$

where $r = |\boldsymbol{x}_{12}|$. The union volume of two spheres for the first three space dimensions is obtained by combining (3.49)–(3.51) with (5.4) to give

$$\frac{v_2(r; R)}{v_1(R)} = 2\Theta(r - 2R) + \Big(1 + \frac{r}{2R}\Big)\Theta(2R - r), \qquad d = 1, \tag{5.8}$$

$$\frac{v_2(r; R)}{v_1(R)} = 2\Theta(r - 2R) + \frac{2}{\pi}\left[\pi + \frac{r}{2R}\Big(1 - \frac{r^2}{4R^2}\Big)^{1/2} - \cos^{-1}\left(\frac{r}{2R}\right)\right]\Theta(2R - r), \quad d = 2, \tag{5.9}$$

$$\frac{v_2(r; R)}{v_1(R)} = 2\Theta(r - 2R) + \left[1 + \frac{3}{4}\frac{r}{R} - \frac{1}{16}\left(\frac{r}{R}\right)^3\right]\Theta(2R - r), \qquad d = 3. \tag{5.10}$$

Note that because the union volume $v_2(r; R)$ becomes constant after one diameter ($r = 2R$), S_2 attains its asymptotic value of ϕ_1^2 for $r \geq 2R$, *independent of the density*. Thus,

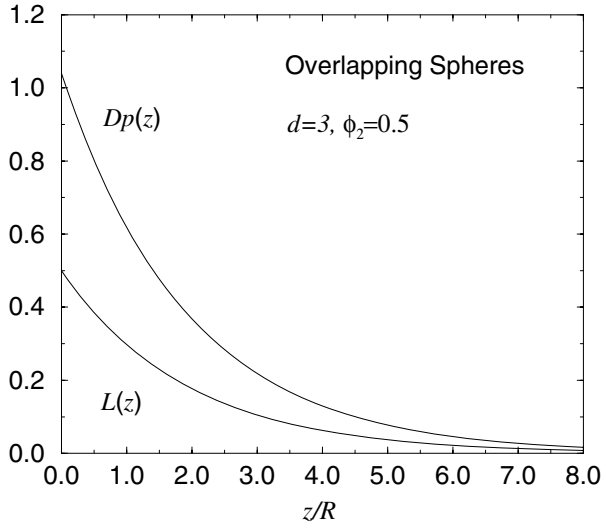

Figure 5.4 Matrix lineal-path function $L(z)$ and chord-length density function $p(z)$ for a three-dimensional system of overlapping spheres of radius R at a sphere volume fraction $\phi_2 = 0.5$, as obtained from (5.23) and (5.26) with $d = 3$.

$$\upsilon_E = \upsilon_1(R; d) + \upsilon_1(R; d-1)z, \tag{5.20}$$

where $\upsilon_1(R; d)$ is the d-dimensional volume of a sphere of radius R given by (4.17). [Note that (5.19) could also have been obtained by setting $n = 0$ and $W = \upsilon_E$ in the Poisson distribution formula (3.19).] Since the matrix volume fraction for fully penetrable spheres is given by $\phi_1 = \exp(-\eta)$, the lineal-path function becomes

$$L(z) = \phi_1^{1 + \frac{\omega_{d-1}}{\omega_d}\frac{z}{R}}, \tag{5.21}$$

where

$$\omega_d \equiv \upsilon_1(1; d) = \frac{\pi^{d/2}}{\Gamma(1 + d/2)} \tag{5.22}$$

is the d-dimensional volume of a sphere of unit radius. For the first three space dimensions (Lu and Torquato 1992a), we have

$$L(z) = \begin{cases} \phi_1^{1 + \frac{1}{2}\frac{z}{R}}, & d = 1, \\ \phi_1^{1 + \frac{2}{\pi}\frac{z}{R}}, & d = 2, \\ \phi_1^{1 + \frac{3}{4}\frac{z}{R}}, & d = 3. \end{cases} \tag{5.23}$$

The case $d = 3$ is plotted in Figure 5.4.

The probability of finding three points in the particle phase can be written as the sum of the probabilities of three different events. The first diagram in (5.42) is the probability that all three points fall in a single sphere. The next three two-body diagrams constitute the probability that one point falls in one particle and the other two points fall in a different particle. These two-body diagrams are not difficult to evaluate using existing accurate analytical approximations for g_2 or via Monte Carlo simulations. Finally, the last diagram is the probability that each point falls in different spheres. It is more problematic to compute, since g_3 is known less precisely than g_2. One can resort to superposition-type approximations for g_3 (Section 3.2) or evaluate the three-body diagram using Monte Carlo methods. The evaluation of S_n for $n \geq 4$ becomes increasingly unwieldy because of the difficulty involved in estimating the g_n (see Section 3.2).

We note in passing that the probability of finding n points at positions $\boldsymbol{r}^n$ in a single sphere of a homogeneous totally impenetrable sphere system is given by

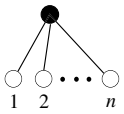

$$= \rho v_n^{\text{int}}(\boldsymbol{r}^n; R) = \rho \int d\boldsymbol{x} \prod_{i=1}^{n} m(|\boldsymbol{r}_i - \boldsymbol{x}|; R), \tag{5.43}$$

where $v_n^{\text{int}}(\boldsymbol{r}^n; R)$ is the intersection volume of n spheres of radius R at positions $\boldsymbol{r}^n$; see also (3.47). The one-body contribution to the n-point probability function $S_n^{(2)}$ is exactly given by diagram (5.43).

Torquato and Lado (1985) found an exact analytical expression for the matrix two-point function $S_2(r_{12})$ for an equilibrium system of hard rods of length D. This was done by direct integration of the two-body diagram in (5.41) and use of the analytical expression for g_2 given by (3.54). After some simplification (Quintanilla and Torquato 1996b), their expression can be written in terms of the dimensionless distance $x = r_{12}/D$ as

$$S_2(x) = (1 - \eta) \sum_{k=0}^{M} \frac{1}{k!} \Big[\frac{(x - k)\eta}{1 - \eta} \Big]^k \exp\Big[- \frac{(x - k)\eta}{1 - \eta} \Big], \tag{5.44}$$

where $M \leq x \leq M + 1$.

In higher dimensions, one can evaluate (5.41) exactly through the first few terms in a density expansion (Torquato and Stell 1985a). However, since g_2 is not known analytically for arbitrary densities for $d \geq 2$, one must necessarily utilize approximations to evaluate the two-body diagram in (5.41). Since the two-body diagram is a double convolution integral, then we can express it, for isotropic media, as

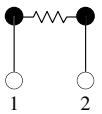

$$= \phi_2^2 + \rho^2 \mathcal{F}^{-1}[\tilde{m}^2 \tilde{h}], \tag{5.45}$$

where $\mathcal{F}^{-1}$ denotes the inverse Fourier transform defined by (2.50), $\tilde{f}(k)$ is the Fourier transform of a function $f(r)$ (see Section 2.2.5), and $h(r) = g_2(r) - 1$ is the total correlation function defined by (3.30). For example, when $d = 3$, we have that

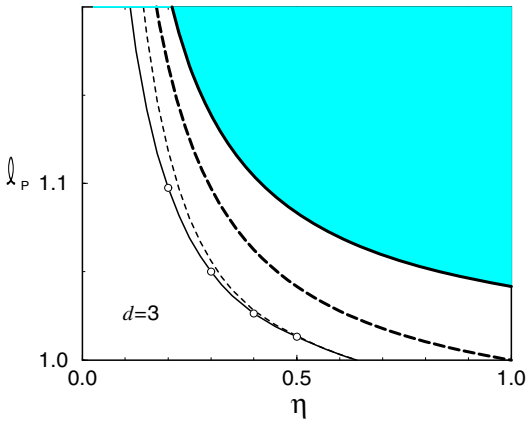

Figure 5.15 Mean nearest-neighbor distance ℓ_P (in units of diameter) versus packing fraction η for a system of hard spheres ($d = 3$). Thin solid line is equilibrium prediction from (2.109) and (5.98); open circles are corresponding simulation data. Thin dashed line is upper bound of Theorem 5.1 for an equilibrium ensemble from (5.107). Thick dashed and solid lines are upper bounds of Theorems 5.2 and 5.3, respectively. Shaded region is prohibited to ergodic, isotropic systems of hard spheres according to Corollary 5.2.

$$\ell_P \le \begin{cases} 1 + \dfrac{(1-\eta)^3}{24\eta(1-\eta/2)}, & 0 \le \eta \le \eta_f, \\ 1 + \dfrac{(\eta_c - \eta)}{24\eta g_f(1)(\eta_c - \eta_f)}, & \eta_f \le \eta \le \eta_c. \end{cases} \tag{5.107}$$

Figure 5.15 also depicts the prediction of the mean nearest-neighbor distance ℓ_P for equilibrium hard spheres ($d = 3$) versus the packing fraction η as computed from definition (2.109) and formula (5.98). This prediction is seen to be in excellent agreement with available simulation data (Torquato and Lee 1990, Rintoul and Torquato 1998). In the limit $\eta \to \eta_c$, this prediction of ℓ_P correctly goes to unity. Included in the figure are the bounds of Theorems 5.1, 5.2, and 5.3. The upper bound of Theorem 5.1 is very sharp (i.e., nearly exact) for packing fractions between freezing and the MRJ state, becoming exact in the limit $\eta \to \eta_c$.

5.2.6 Pore-Size Functions

Torquato and Avellaneda (1991) used interrelation (2.84) and the approximate expression for $H_V(r)$ for hard spheres given by Torquato et al. (1990) to get the pore-size functions $P(\delta)$ and $F(\delta)$. Slightly more accurate expressions for these functions can be obtained using (5.91). The results from this latter approximation for $P(\delta)$ are plotted in Figure 5.16 for $\phi_2 = 0.5$. Included in the figure are corresponding results for two other values of the impenetrability parameter λ in the cherry-pit model (Section 3.1.2): $\lambda = 0$

6.2.3 Lineal-Path Function

For the same reasons as in the monodisperse case (see Section 5.2.3), the series (6.19) cannot be evaluated exactly for $d \geq 2$. Lu and Torquato (1992c) found *scaled-particle* approximations of the lineal-path function $L(z) \equiv L^{(1)}(z)$ for the matrix phase of a system of polydisperse hard spheres in equilibrium. These results in any dimension d are given by

$$L(z) = \phi_1 \exp\left[-\frac{\eta\, \omega_{d-1}\langle R^{d-1}\rangle}{\phi_1 \omega_d \langle R^d\rangle} z\right]. \tag{6.36}$$

For the first three space dimensions (Lu and Torquato 1992c), we have

$$L(z) = \begin{cases} \phi_1 \exp\Big[-\dfrac{\eta}{2\phi_1\langle R\rangle} z\Big], & d = 1, \\ \phi_1 \exp\Big[-\dfrac{2\eta\langle R\rangle}{\pi\phi_1\langle R^2\rangle} z\Big], & d = 2, \\ \phi_1 \exp\Big[-\dfrac{3\eta\langle R^2\rangle}{4\phi_1\langle R^3\rangle} z\Big], & d = 3. \end{cases} \tag{6.37}$$

Whereas the expression for $d = 1$ is exact, the other expressions are accurate approximations. As in the case of overlapping spheres, we see that if one scales the distance z in (6.36) by the length $\langle R^d\rangle/\langle R^{d-1}\rangle$ (proportional to the average volume-to-surface ratio of a sphere), results for $L(z)$ for any polydispersivity collapse onto the monodisperse curve [cf. (5.58)]. This turns out to be true for relation (6.38) for the chord-length distribution function $p(z)$. Therefore, Figure 5.8 for the monodisperse case also depicts the corresponding polydisperse results when z is scaled in this manner.

6.2.4 Chord-Length Density Function

The chord-length density function $p(z) \equiv p^{(1)}(z)$ for the matrix phase of systems of polydisperse equilibrium hard spheres is easily obtained using expressions (2.68), (2.73), and (6.36):

$$p(z) = \frac{\eta\, \omega_{d-1}\langle R^{d-1}\rangle}{\phi_1 \omega_d \langle R^d\rangle} \exp\Big[-\frac{\eta\, \omega_{d-1}\langle R^{d-1}\rangle}{\phi_1\, \omega_d \langle R^d\rangle} z\Big]. \tag{6.38}$$

Thus, in the first three space dimensions (Torquato and Lu 1993), we have

$$p(z) = \begin{cases} \dfrac{\eta}{2\phi_1\langle R\rangle} \exp\Big[-\dfrac{\eta}{2\phi_1\langle R\rangle} z\Big], & d = 1, \\ \dfrac{2\eta\langle R\rangle}{\pi\phi_1\langle R^2\rangle} \exp\Big[-\dfrac{2\eta\langle R\rangle}{\pi\phi_1\langle R^2\rangle} z\Big], & d = 2, \\ \dfrac{3\eta\langle R^2\rangle}{4\phi_1\langle R^3\rangle} \exp\Big[-\dfrac{3\eta\langle R^2\rangle}{4\phi_1\langle R^3\rangle} z\Big], & d = 3. \end{cases} \tag{6.39}$$

The corresponding explicit expressions for the mean chord lengths are

$$\ell_C = \frac{\phi_1\ \omega_d \langle R^d \rangle}{\eta\ \omega_{d-1} \langle R^{d-1} \rangle} = \frac{\omega_d\ \phi_1 d}{\omega_{d-1}}\ \frac{1}{s}, \tag{6.40}$$

where we have used formula (6.33) for the specific surface s.

6.2.5 Nearest-Surface Functions

Using the definition (4.90) and series (4.81) for the canonical function H_n gives the following series representation of the void nearest-surface exclusion probability function for any statistically homogeneous ensemble of totally impenetrable polydisperse spheres:

$$e_V(r) = 1 + \sum_{k=1}^{\infty} (-1)^k \frac{1}{k!} \int \cdots \int dR_1 \cdots dR_k f(R_1) \cdots f(R_k) \times \rho_k(\boldsymbol{r}^k; R_1, \ldots, R_k) \prod_{j=1}^{k} m(|\boldsymbol{x} - \boldsymbol{r}_j|; r) d\boldsymbol{r}_j, \tag{6.41}$$

where $m(y; r) = \Theta(r + R - y)$. Similarly, the corresponding relation for the particle nearest-surface exclusion probability is obtained from (4.91) and (4.81), yielding

$$e_P(r) = 1 + \sum_{k=1}^{\infty} (-1)^k \frac{1}{\rho k!} \int \cdots \int dR_1 \cdots dR_{k+1} f(R_1) \cdots f(R_{k+1}) \times \rho_{k+1}(\boldsymbol{r}^{k+1}; R_1, \ldots, R_{k+1}) \prod_{j=2}^{k+1} m(|\boldsymbol{r}_1 - \boldsymbol{r}_j|; r) d\boldsymbol{r}_j. \tag{6.42}$$

The results (6.41) and (6.42) were first given by Lu and Torquato (1992b). The series expressions for the other nearest-surface quantities are found using the above expressions for the exclusion probabilities and interrelations (2.115) and (2.116).

The nearest-surface quantities must obey certain exact conditions for totally impenetrable spheres *in any ensemble*. In the case of the particle quantities, the *reference* particle of radius R excludes the surface of any other particles from a sphere of radius R, and therefore we have

$$e_P(r) = 1, \qquad h_P(r) = g_P(r) = 0, \qquad 0 \le r \le R. \tag{6.43}$$

In the case of the void quantities, the reference point can only be inside one of the particles, and hence the void nearest-surface exclusion probability and probability density function for all allowable negative values of r (see Sections 2.8 and 6.1.5) are given respectively by

$$e_V(r) = 1 - \rho \langle \upsilon_1(r + R) \Theta(r + R) \rangle, \qquad r < 0, \tag{6.44}$$

$$h_V(r) = \rho \langle s_1(r + R) \Theta(r + R) \rangle, \qquad r < 0. \tag{6.45}$$

The function g_V is just the ratio h_V/e_V, and henceforth for brevity we will just report results for e_V and h_V.

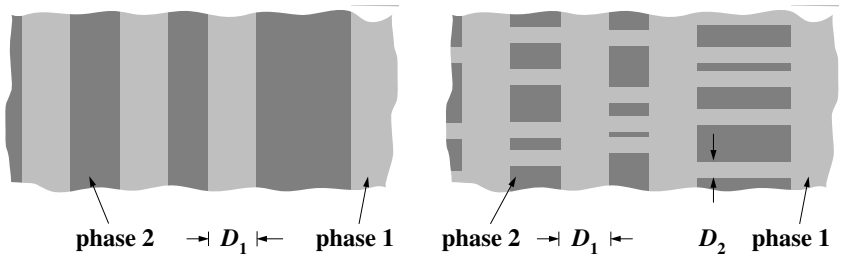

Figure 7.4 Schematics of two-dimensional laminates. Left panel: A portion of a random rank 1 laminate. Right panel: A portion of a random rank 2 laminate.

A *random* first-rank laminate is made by alternating layers of phase 1 and phase 2 materials according to some random process, as shown in Figure 7.4. A random second-rank laminate is constructed in two stages. For simplicity, the first stage is taken to be a series of parallel slabs of *fixed* width D_1 oriented in the y-direction generated by some one-dimensional random process. We define $\phi_1^{(1)}$ and $\phi_2^{(1)}$ to be the volume fractions of the matrix phase (phase 1) and the included phase (phase 2), respectively. The second stage of lamination adds *perpendicular* slabs of width D_2 in the gaps of the first stage. We define $\phi_1^{(2)}$ and $\phi_2^{(2)}$ to be the volume fractions of phases 1 and 2, respectively, for the second-stage process (see Figure 7.4). Clearly,

$$\phi_1^{(1)} + \phi_2^{(1)} = \phi_1^{(2)} + \phi_2^{(2)} = 1. \tag{7.24}$$

Moreover, a point lies in phase 2 of the *entire laminate* exactly when its x-coordinate lies in phase 2 of the first stage and its x-coordinate lies in phase 2 of the second stage of lamination. Since these events are independent, we see that the volume fraction of phase 2 of the entire laminate is given by

$$\phi_2 = 1 - \phi_1 = \phi_2^{(1)}\phi_2^{(2)}. \tag{7.25}$$

Useful one-dimensional models from which laminates can be constructed include fully penetrable rods, totally impenetrable rods, and one-dimensional "random checkerboards." Realizations of these three systems are shown in Figure 7.5; the systems depicted have equal rod lengths and volume fractions of the phases. By a one-dimensional "checkerboard" process we mean systems in which the line is divided into equisized sections of width D. Each section, independent of the other sections, belongs to phase 1 with probability ϕ_1 and phase 2 with probability ϕ_2. (The checkerboard model in higher dimensions is discussed in detail in Section 8.1.4.) By extending these one-dimensional systems into higher dimensions, hierarchical laminates are constructed.

Quintanilla and Torquato (1996b) showed that the two-point probability function for phase 1 for two-dimensional second-rank laminates of arbitrary construction is given by

$$S_2(\boldsymbol{r}) = L^{(1)}(x)S_2^{(2)}(y) + [S_2^{(1)}(x) - L^{(1)}(x)](\phi_1^{(2)})^2. \tag{7.26}$$

1997). The characterization of the microstructure of random cellular materials is an interesting problem and has been attacked from a variety of viewpoints.

Below we define and discuss the Voronoi and Delaunay tessellations. This is followed by a brief description of certain cell statistics. We then discuss the n-point probability functions for *symmetric-cell* materials in general and the *random checkerboard* model in particular.

8.1.1 Voronoi and Delaunay Tessellations

A *Voronoi tessellation* is a certain fundamental partitioning (tiling) of d-dimensional space into d-dimensional polyhedral cells (polytopes). This construction is also known to mathematicians as a *Dirichlet tessellation*. Condensed-matter physicists refer to the cells as *Wigner–Seitz* cells. The Voronoi tessellation and its dual (the Delaunay tessellation) have been reinvented, given different names, generalized, and applied in numerous different fields, including biology, meteorology, metallurgy, crystallography, forestry, ecology, archaeology, geology, geography, astrophysics, physics, computer science, and engineering (Aurenhammer 1991, Okabe, Boots and Sugihara 1992).

Consider a set of N points or sites with positions $\boldsymbol{r}_1, \boldsymbol{r}_2, \ldots, \boldsymbol{r}_N$ in volume V in d spatial dimensions. This set of positions may be deterministic (e.g., regular lattice) or random. Associated with the ith point at $\boldsymbol{r}_i$ is the *Voronoi cell*, which is defined to be the region of space nearer to the point at $\boldsymbol{r}_i$ than to any other point in the set. In two dimensions such a cell is a convex polygon, whereas in three dimensions such a cell is a convex polyhedron. In two dimensions, the boundary of the Voronoi polygon is composed of segments of the perpendicular bisectors of each line (edge) that connects the point at $\boldsymbol{r}_i$ to its *nearest-neighbor* sites (points that share a Voronoi edge). An example is indicated in Figure 8.1. In three dimensions, the boundary of the Voronoi polyhedron is composed of planes that perpendicularly bisect each edge that connects the point at $\boldsymbol{r}_i$ to its nearest-neighbor sites (points that share a Voronoi face). We refer to the set of all Voronoi cells associated with the N points as a *Voronoi diagram*. A Voronoi diagram becomes a *Voronoi tessellation* when it extends to all of space. This extension can be accomplished by taking the *thermodynamic limit* (see Section 3.1) or by the use of periodic boundary conditions so that the volume V is surrounded by images of itself *ad infinitum*.

Before discussing the Delaunay tessellation, it is useful to recall a few *topological* definitions and results. Generally speaking, a *graph* is a *topological* object composed of vertices and lines (or edges) connecting some subset of the vertices. A *polyhedral* graph G is one in which each edge belongs to the *face* of a polyhedron. Therefore, the network of edges (or bonds) that constitute the Voronoi tessellation is a special polyhedral graph. In any graph, the number of edges joined to a particular vertex is its *coordination number* Z. The *dual* graph G^* of a polyhedral graph G has vertices each of which corresponds to a face of G and each of whose faces corresponds to a vertex of G. Finally, for any subdivision of a domain into a finite number of polyhedral cells C, one can relate the number of vertices V, the number of edges E, and the number of

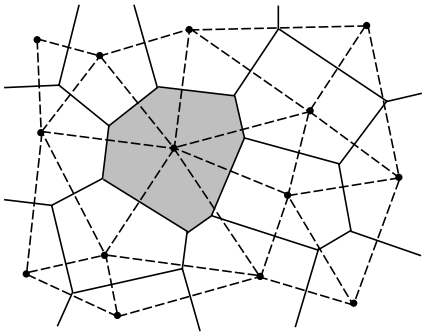

Figure 8.1 Voronoi and Delaunay tessellations for points (black dots) in the plane. The Voronoi polygons are indicated with solid lines, while the Delaunay triangles are indicated with dashed lines.

faces F to each other via Euler's formula:

$$F - E + V = 1, \qquad \text{(two-dimensional Euclidean space)}, \tag{8.1}$$

$$F - E + V - C = 1, \qquad \text{(three-dimensional Euclidean space)}. \tag{8.2}$$

Euler's formula has also been generalized to non-Euclidean spaces (e.g., the surface of a sphere or torus). It can be viewed as a *conservation* law, since it applies even if the structure is evolving with time.

Given a Voronoi graph, the *Delaunay graph* results from joining all pairs of sites that share a Voronoi face (nearest-neighbor sites) and divides all space into polyhedra. This subdivision of space is called the *Delaunay tessellation*, and it is the unique dual of the Voronoi tessellation. If the Delaunay tessellation consists only of simplices, i.e., simplest polyhedra (triangles in two dimensions and a tetrahedra in three dimensions), then we call it a *Delaunay triangulation*. If not, the Delaunay tessellation can still be triangulated, but the resulting triangulation is no longer unique. We note that for random point patterns, the Delaunay tessellation is almost always a triangulation of the space, except for some rare symmetric subset of points.

Let us now consider some specific point patterns that lead to Voronoi tessellations and may be used to model cellular materials. We will first give examples of *regular* point patterns (in two and three dimensions) that result in cells of regular shape. In two dimensions, there are many regular point patterns that one can choose from, but for simplicity we will limit ourselves to some well-known patterns resulting in cells of identical shape and size that tile the plane. As shown in Figure 8.2, points arranged on a regular *triangular lattice* lead to Voronoi cells that are *regular hexagons*. (Note that the corresponding Delaunay tessellation is the regular triangular graph.) The Voronoi cells associated with points arranged on a *regular honeycomb lattice* are *regular triangles*. Thus, the triangular-lattice graph is the dual of the honeycomb-lattice graph. (Observe that the Delaunay tessellation of the honeycomb lattice is not a triangulation.) Since

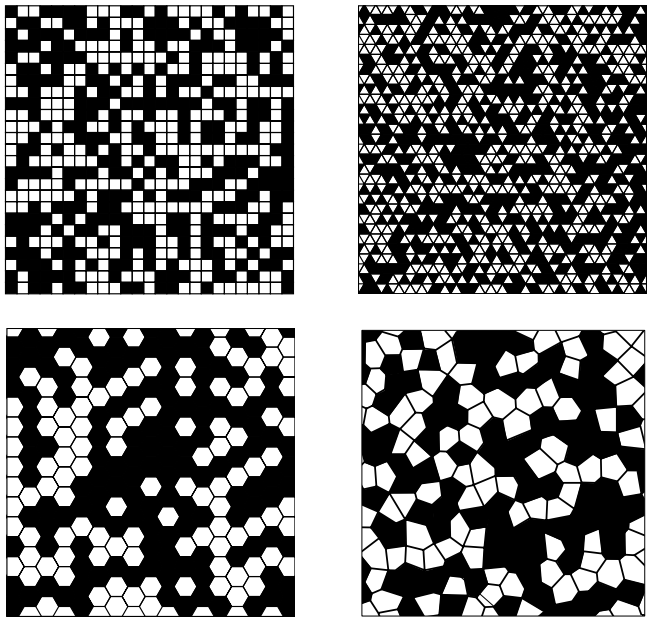

Figure 8.5 Four examples of two-dimensional two-phase symmetric-cell materials at the area fraction $\phi_1 = \phi_2 = 0.5$. Top left: Square cells (random checkerboard model). Top right: Triangular cells. Bottom left: Hexagonal cells. Bottom right: Randomly shaped cells generated from RSA hard-disk centers.

probability density function ρ_n.] We will also make some specific remarks about the two- and three-point quantities. The derivation below is considerably simpler than the one given by Miller (1969) and more general (he considered only the three-point quantity).

n-Point Probability Function

Let $S_n(\boldsymbol{x}^n) \equiv S_n^{(1)}(\boldsymbol{x}^n)$ and $\hat{S}_n(\boldsymbol{x}^n) \equiv S_n^{(2)}(\boldsymbol{x}^n)$ denote the probability that n points at positions $\boldsymbol{x}^n \equiv \{\boldsymbol{x}_1, \boldsymbol{x}_2, \ldots, \boldsymbol{x}_n\}$ fall in the white phase and black phase, respectively. Then we can express the n-point quantities as

$$S_n(\boldsymbol{x}^n) = \sum_{k=1}^{n} P_n^{(k)}(\boldsymbol{x}^n), \qquad \text{for all } n, \tag{8.11}$$

$$\hat{S}_n(\boldsymbol{x}^n) = \sum_{k=1}^{n} \hat{P}_n^{(k)}(\boldsymbol{x}^n), \qquad \text{for all } n, \tag{8.12}$$

where, for any $1 \le k \le n$,

$$P_n^{(k)} = \text{Probability that } n \text{ points fall in } k \text{ different white cells}, \tag{8.13}$$

$$\hat{P}_n^{(k)} = \text{Probability that } n \text{ points fall in } k \text{ different black cells}. \tag{8.14}$$

and

$$V_S = \frac{\sum_{k=1}^{\infty} k n_k V_k}{\sum_{k=1}^{\infty} k n_k} = \sum_{k=1}^{\infty} k n_k V_k. \tag{9.37}$$

Here V_Q is the "average cluster volume," or the average volume of a randomly chosen cluster. The quantity V_S is the "particle-averaged cluster volume," or the average volume of the cluster containing a randomly chosen particle.

The percolation probability $P(\phi_2)$ is the probability that an arbitrarily selected particle belongs to the infinite cluster. Therefore, for an infinite system,

$$P(\phi_2) \begin{cases} = 0, & \text{if} \quad \phi_2 < \phi_{2c}, \\ > 0, & \text{if} \quad \phi_2 > \phi_{2c}. \end{cases} \tag{9.38}$$

The *percolation-threshold value* ϕ_{2c} is defined formally as $\phi_{2c} = \sup\{\phi_2 : P(\phi_2) = 0\}$ and, for the same reasons given in Section 9.1.1, is a *nonuniversal* quantity. Note that $P(\phi_2)$ is equivalent to the fraction of the particle-phase volume fraction ϕ_2 that is connected.

The pair-connectedness function $P_2(r)$ can be obtained for a general isotropic system of spheres by decomposing the radial distribution function $g_2(r)$ defined in Chapter 3 into a "connected" part and a "disconnected" part (Coniglio, De Angelis and Forlani 1977), i.e.,

$$g_2(r) = P_2(r) + B_2(r), \tag{9.39}$$

where

$$\rho^2 P_2(r) = \text{Probability density function associated with finding two particles (whose centers are separated by a distance } r\text{) in the same cluster,} \tag{9.40}$$

$$\rho^2 B_2(r) = \text{Probability density function associated with finding two particles (whose centers are separated by a distance } r\text{) } \textit{not} \text{ in the same cluster.} \tag{9.41}$$

The quantity $B_2(r)$ is referred to as the *pair-blocking* function. The decomposition (9.39) is elaborated on in Section 10.2.

The mean cluster size S is related to the pair-connectedness function P_2 via the expression (Coniglio et al. 1977)

$$S = 1 + \rho \int P_2(r) d\boldsymbol{r}. \tag{9.42}$$

This relation is completely analogous to the *compressibility equation* (3.15) that arises in the study of the liquid state. Note that the asymptotic form of $P_2(r)$ for large r at the percolation threshold is still given by (9.7) and thus ensures that the mean cluster size (9.42) will diverge when $\phi_2 = \phi_{2c}$.

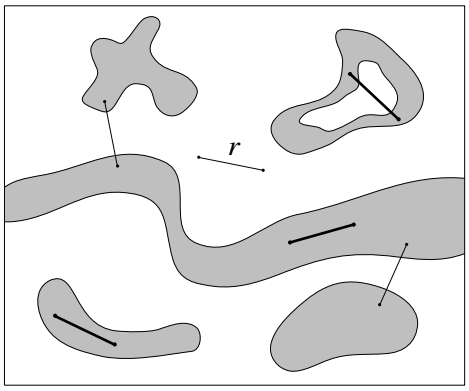

Figure 9.11 Two possible ways in which the end points of a line segment of length r can land in phase 2 (gray region) when randomly tossed into an isotropic medium: (1) end points fall in the same cluster (bold lines) or (2) end points fall in different clusters (lighter lines).

The quantity E_2 is called the *two-point blocking function*.

Clearly, C_2 generally contains nontrivial connectedness information and therefore is a better signature of the microstructure than S_2. To emphasize this point, Figure 9.11 schematically depicts an arbitrary isotropic continuum model in which lines of length $r = |\boldsymbol{x}_2 - \boldsymbol{x}_1|$ are shown. The bold lines represent events that contribute only to $C_2(r)$, whereas all of the lines (bold and lighter ones), except the one falling entirely in the matrix, represent events that contribute to $S_2(r)$. This clearly shows that S_2 generally does not distinguish between clustering and nonclustering events. One exception to this would be systems containing a very few but fractal clusters. For a single fractal cluster (e.g., the diffusion-limited aggregation cluster discussed in Chapter 12), $S_2(r) = C_2(r)$ falls off as $r^{d_F - d}$ (Family 1993), and therefore the corresponding Fourier transform or scattering intensity $i(k)$ (Section 2.2.5) scales as k^{-d_F} (Thompson et al. 1987), where d_F is the fractal dimension. The quantity C_2 is discussed further in Chapter 10.

9.2.3 Critical Exponents

Near criticality, the quantities P, S, and ξ have the same type of scaling behavior as in lattice percolation, i.e.,

$$P \sim (\phi_2 - \phi_{2c})^{\beta}, \qquad \phi_2 \to \phi_{2c}^{+}, \tag{9.46}$$

$$S \sim |\phi_2 - \phi_{2c}|^{-\gamma}, \qquad \phi_2 \to \phi_{2c}, \tag{9.47}$$

$$\xi \sim |\phi_2 - \phi_{2c}|^{-\nu}, \qquad \phi_2 \to \phi_{2c}. \tag{9.48}$$

For the model of overlapping particles of various shapes, many previous studies (Haan and Zwanzig 1977, Gawlinski and Stanley 1981, Kertesz and Vicsek 1982, Elam, Kerstein and Rehr 1984, Lorenz, Orgzall and Heuer 1993) have indicated that the geometrical critical exponents, β, γ, and ν, are in the same universality class as lat-

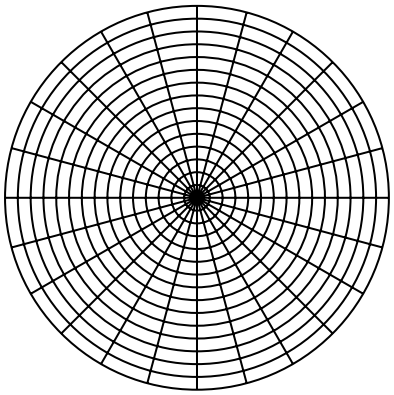

Figure 12.11 A template to sample for S_2 or S_3 in two-dimensional homogeneous media. The grid spacing need not be regular as shown here.

This process is repeated for each realization, and the final result for S_1 is obtained by averaging over all realizations. Execution speed to check the overlap condition (12.10) can be increased significantly using a *cell list* (Haile et al. 1985), which identifies the sphere centers that are in some small subvolume of the system. When the randomly placed point lands in a particular subvolume, then condition (12.10) is checked only for those centers located in the subvolume and its immediate neighboring subvolumes. The one-point function S_1 has been evaluated from simulations for spheres in the cherry-pit model as a function of the impenetrability parameter (Lee and Torquato 1988a).

For statistically homogeneous but anisotropic particle systems (e.g., oriented ellipsoids or cylinders), it is better to compute the two-point function $S_2(\boldsymbol{r})$ (where $\boldsymbol{r} = \boldsymbol{x}_2 - \boldsymbol{x}_1$) by randomly tossing many line segments of length $r = |\boldsymbol{r}|$ with *fixed orientation* (specified by the vector $\boldsymbol{r}$) into each realization, measuring the fraction of times that both ends of the line segment lie outside the particles, and averaging over all realizations. For statistically isotropic media, $S_2(r)$ is found in the same way except that the line segments are randomly oriented.

For both isotropic and anisotropic (but homogeneous) d-dimensional media, efficiency can be improved by randomly tossing a "sampling template" consisting of a grid of many points (Smith and Torquato 1988), as depicted in Figure 12.11 for $d = 2$. Many line segments (in which one end is always at the template origin) of variable lengths and orientations are contained in a template. Sampling templates at many locations (say 10,000 or more) are used to sample each realization. This will yield the two-point function $S_2(\boldsymbol{r})$ that will depend on the vector displacement $\boldsymbol{r}$ for anisotropic media. If the medium is isotropic, then $S_2(r)$ will depend only on the distance $r = |\boldsymbol{r}|$ and hence is obtained by averaging over all orientations of $\boldsymbol{r}$. The function S_2 has been computed for equilibrium hard spheres (Haile et al. 1985) and RSA disks in the cherry-pit model (Smith and Torquato 1988).

$$\varepsilon_{11} = 0, \quad \varepsilon_{22} = \varepsilon_{33} = \varepsilon.$$

Letting

$$\tau_{22} = \tau_{33} = \tau,$$

we find from (13.74) that

$$\tau = 2k_{23}\varepsilon,$$

where

$$k_{23} = \frac{1}{2}(C_{22} + C_{23}) \tag{13.75}$$

is the *plane strain* or *transverse* bulk modulus.

Now consider a simple state of uniaxial stress, i.e.,

$$\tau_{11} \neq 0, \quad \tau_{22} = \tau_{33} = \tau_{12} = \tau_{23} = \tau_{13} = 0.$$

For such a state, (13.74) reveals that

$$\tau_{11} = E_{11}\varepsilon_{11},$$

where

$$E_{11} = C_{11} - \frac{2C_{12}^2}{C_{22} + C_{23}} \tag{13.76}$$

is the *longitudinal* Young's modulus. The Poisson ratios that characterize the typical lateral contraction (expansion) that accompanies uniaxial tension (compression) in the x_1-direction are defined by the relations

$$\nu_{12} = -\frac{\varepsilon_{22}}{\varepsilon_{11}}, \qquad \nu_{13} = -\frac{\varepsilon_{33}}{\varepsilon_{11}}.$$

Generally, ν_{ij} is Poisson's ratio, where the first index i indicates the direction of the imposed stress or strain and the second index j indicates the response direction. For the aforementioned uniaxial stress state, we have from (13.74) that

$$\nu_{12} = \nu_{13} = \frac{C_{12}}{C_{22} + C_{23}}. \tag{13.77}$$

The directly measurable shear moduli are defined in the usual way, i.e.,

$$G_{12} = G_{13} = C_{66}, \tag{13.78}$$

$$G_{23} = \frac{1}{2}(C_{22} - C_{23}). \tag{13.79}$$

Using the relations above, we can express the five coefficients of (13.73) in terms of the directly measurable moduli:

$$C_{11} = E_{11} + 4\nu_{12}^2 k_{23}, \qquad C_{12} = 2k_{23}\nu_{12},$$
$$C_{22} = k_{23} + G_{23}, \qquad C_{23} = k_{23} - G_{23}, \qquad C_{66} = G_{12}.$$

Here $p(\boldsymbol{x}, t)$ is the pressure, ρ is the constant fluid density, ν is the kinematic viscosity, υ_0 is a constant speed, $\boldsymbol{e}$ is an arbitrary unit vector in the direction of the applied field, and $\delta(t)$ is the Dirac delta function. It will be implicit in all of the ensuing discussion that we assume a zero-traction condition at the boundary of $\mathcal{V}$.

The solution of (13.210)–(13.212) can be expressed as a sum of normal modes as follows:

$$\frac{\boldsymbol{v}(\boldsymbol{x}, t)}{\upsilon_0} = \sum_{n=1}^{\infty} b_n e^{-t/\Theta_n} \boldsymbol{\Psi}_n(\boldsymbol{x}), \tag{13.213}$$

where the vector eigenfunctions $\boldsymbol{\Psi}_n$ satisfy

$$\Delta \boldsymbol{\Psi}_n + \nabla Q_n = -\epsilon_n \boldsymbol{\Psi}_n \qquad \text{in } \mathcal{V}_1(\omega), \tag{13.214}$$

$$\nabla \cdot \boldsymbol{\Psi}_n = 0 \qquad \text{in } \mathcal{V}_1(\omega), \tag{13.215}$$

$$\boldsymbol{\Psi}_n = 0 \qquad \text{on } \partial\mathcal{V}(\omega). \tag{13.216}$$

Here the $\Theta_n = 1/(\nu\epsilon_n)$ are viscous relaxation times, and so the nth eigenvalue ϵ_n has dimensions of (length)$^{-2}$. The functions Q_n in (13.214) are the corresponding pressures. The eigenfunctions $\boldsymbol{\Psi}_n$ are orthonormal, so that

$$\frac{1}{V_1} \int_{\mathcal{V}_1} \boldsymbol{\Psi}_m(\boldsymbol{x}) \cdot \boldsymbol{\Psi}_n(\boldsymbol{x}) d\boldsymbol{x} = \delta_{mn}, \tag{13.217}$$

and the eigenfunction expansion coefficients are given by

$$b_n = \frac{1}{V_1} \int_{\mathcal{V}_1} \boldsymbol{e} \cdot \boldsymbol{\Psi}_n(\boldsymbol{x}) d\boldsymbol{x}. \tag{13.218}$$

Here $V_1 = \phi_1 V$ denotes the total pore volume.

Note that the set of orthonormal eigenfunctions $\boldsymbol{\Psi}_n$ is complete in the closed subspace of square integrable divergence-free fields having zero normal component on $\partial\mathcal{V}$ (Temam 1979). According to the classical Hodge decomposition (Temam 1979), we can express the constant unit vector $\boldsymbol{e}$ as the sum of a solenoidal field, with vanishing normal component on the pore–solid interface, and the gradient of a potential, as follows:

$$\boldsymbol{e} = \boldsymbol{E} + \nabla\varphi. \tag{13.219}$$

Here $\boldsymbol{E}$ is a dimensionless field satisfying

$$\nabla \cdot \boldsymbol{E} = 0 \qquad \text{in } \mathcal{V}_1(\omega), \tag{13.220}$$

$$\boldsymbol{E} \cdot \boldsymbol{n} = 0 \qquad \text{on } \partial\mathcal{V}(\omega), \tag{13.221}$$

where $\boldsymbol{n}$ is the unit outward normal from the pore region. Relation (13.219) implies that

$$\nabla \times \boldsymbol{E} = 0 \qquad \text{in } \mathcal{V}_1(\omega). \tag{13.222}$$

We observe that the field $\boldsymbol{E}$ then solves the corresponding electric conduction problem for a porous medium filled with a conducting fluid of conductivity σ_1 and having an

(1968) demonstrated how to extend variational principles for the conductivity of homogeneous bodies with prescribed homogeneous boundary conditions to variational principles for the effective conductivity of random media. The minimum principles given below follow Beran's approach, but we give more details and treat boundary terms differently.

Theorem 14.3 *Minimum Potential Energy:*
Let A_U be the class of trial intensity fields $\hat{\boldsymbol{E}}$ defined by the set

$$A_U = \{\text{ergodic } \hat{\boldsymbol{E}};\ \nabla \times \hat{\boldsymbol{E}} = 0,\ \langle \hat{\boldsymbol{E}} \rangle = \langle \boldsymbol{E} \rangle\}, \tag{14.37}$$

and let

$$W[\hat{\boldsymbol{E}}] = \frac{1}{2}\langle \hat{\boldsymbol{E}}(\boldsymbol{x}) \cdot \boldsymbol{\sigma}(\boldsymbol{x}) \cdot \hat{\boldsymbol{E}}(\boldsymbol{x}) \rangle \tag{14.38}$$

be the trial energy functional, where $\boldsymbol{\sigma}$ is the local conductivity tensor. Then, among all trial fields $\hat{\boldsymbol{E}}$, the field that makes the associated flux solenoidal is the one that uniquely minimizes the trial energy functional $W[\hat{\boldsymbol{E}}]$. In other words,

$$W[\boldsymbol{E}] \leq W[\hat{\boldsymbol{E}}] \qquad \forall \hat{\boldsymbol{E}} \in A_U, \tag{14.39}$$

or, equivalently,

$$\frac{1}{2}\langle \boldsymbol{E} \rangle \cdot \boldsymbol{\sigma}_e \cdot \langle \boldsymbol{E} \rangle \leq \frac{1}{2}\langle \hat{\boldsymbol{E}} \cdot \boldsymbol{\sigma} \cdot \hat{\boldsymbol{E}} \rangle \qquad \forall \hat{\boldsymbol{E}} \in A_U, \tag{14.40}$$

where $\boldsymbol{E}$ satisfies (14.14).

Proof: Let the "difference" field $\boldsymbol{G}$ be defined by

$$\boldsymbol{G} = \hat{\boldsymbol{E}} - \boldsymbol{E}$$

such that the trial field $\hat{\boldsymbol{E}}$ satisfies

$$\nabla \times \hat{\boldsymbol{E}} = 0, \quad \langle \hat{\boldsymbol{E}} \rangle = \langle \boldsymbol{E} \rangle.$$

Thus, $\langle \boldsymbol{G} \rangle = 0$, and since both $\boldsymbol{E}$ and $\hat{\boldsymbol{E}}$ are irrotational, $\boldsymbol{G}$ is also irrotational, implying that it can be written as the gradient of a scalar ϕ, i.e.,

$$\boldsymbol{G} = -\nabla\phi.$$

Consider the identity

$$\langle \hat{\boldsymbol{E}} \cdot \boldsymbol{\sigma} \cdot \hat{\boldsymbol{E}} \rangle = \langle \boldsymbol{E} \cdot \boldsymbol{\sigma} \cdot \boldsymbol{E} \rangle + 2\langle \boldsymbol{G} \cdot \boldsymbol{\sigma} \cdot \boldsymbol{E} \rangle + \langle \boldsymbol{G} \cdot \boldsymbol{\sigma} \cdot \boldsymbol{G} \rangle.$$

We now prove that the middle term of this identity is identically zero. Formula (14.8) for integration by parts with $\boldsymbol{A} = \phi$ and $\boldsymbol{B} = \boldsymbol{J} = \boldsymbol{\sigma} \cdot \boldsymbol{E}$ gives

$$\begin{aligned} \langle \boldsymbol{G} \cdot \boldsymbol{\sigma} \cdot \boldsymbol{E} \rangle &= -\langle \nabla\phi \cdot \boldsymbol{J} \rangle \\ &= -\lim_{V\to\infty} \frac{1}{V} \int_S \phi(\boldsymbol{J} \cdot \boldsymbol{n}) dS + \lim_{V\to\infty} \frac{1}{V} \int_V \phi(\nabla \cdot \boldsymbol{J}) dV \\ &= -\lim_{V\to\infty} \frac{1}{V} \int_S \phi'(\boldsymbol{J}' \cdot \boldsymbol{n}) dS = 0. \end{aligned} \tag{14.41}$$

The third line of (14.41) follows after decomposing ϕ and J into their mean and fluctuating parts (as in the proof of Theorem 14.1), using the condition $\langle \boldsymbol{G} \rangle = 0$, and employing the fact that $\boldsymbol{J}$ is solenoidal. The integral in the third line of (14.41) involving the fluctuating fields is zero by ergodicity. Using this result in combination with energy representation (14.31) gives

$$\langle \hat{\boldsymbol{E}} \cdot \boldsymbol{\sigma} \cdot \hat{\boldsymbol{E}} \rangle = \langle \boldsymbol{E} \rangle \cdot \boldsymbol{\sigma}_e \cdot \langle \boldsymbol{E} \rangle + \langle \boldsymbol{G} \cdot \boldsymbol{\sigma} \cdot \boldsymbol{G} \rangle,$$

and since the second term on the right side is greater than or equal to zero, the statement (14.40) is proved. The equality sign holds only when the difference field $\boldsymbol{G}$ is zero throughout $\mathcal{V}$, i.e., when $\hat{\boldsymbol{E}} = \boldsymbol{E}$.

If there were another field $\boldsymbol{E}^*$ from the set A_U, different from $\boldsymbol{E}$ but with a solenoidal flux, then we could apply the above theorem first to $\boldsymbol{E}^*$ and then to $\boldsymbol{E}$, yielding the contradictory results that $W[\boldsymbol{E}^*] > W[\boldsymbol{E}]$ and $W[\boldsymbol{E}] > W[\boldsymbol{E}^*]$; therefore, $\boldsymbol{E}$ is unique. ∎

Remarks:

1. In words, the minimum potential principle states that the actual macroscopic energy $W[\boldsymbol{E}]$ is bounded from above by the trial macroscopic energy $W[\hat{\boldsymbol{E}}]$ and thus leads to an upper bound $\boldsymbol{\sigma}_e^U$ on the effective conductivity tensor $\boldsymbol{\sigma}_e$ in the positive semidefinite sense [cf. (13.16)].
2. Theorem 14.3 applies as well to periodic media (Bensoussan et al. 1978). Boundary terms are now over the unit cell and vanish because of periodicity.
3. In the parlance of variational calculus, the difference field $\boldsymbol{G}$ (defined in the proof above) is the *first variation* of the trial field, denoted by $\delta\hat{\boldsymbol{E}}$. One seeks the minimizer of the first variation of the trial energy functional, which we have done. Throughout this chapter, however, we will avoid this language and notation, since it is less accessible to the nonspecialist.

Theorem 14.4 *Minimum Complementary Energy:*
Let A_L be the class of trial flux fields $\hat{\boldsymbol{J}}$ defined by the set

$$A_L = \{\text{ergodic } \hat{\boldsymbol{J}}; \nabla \cdot \hat{\boldsymbol{J}} = 0,\ \langle \hat{\boldsymbol{J}} \rangle = \langle \boldsymbol{J} \rangle\}, \tag{14.42}$$

and let

$$W[\hat{\boldsymbol{J}}] = \frac{1}{2}\langle \hat{\boldsymbol{J}}(\boldsymbol{x}) \cdot \boldsymbol{\sigma}^{-1}(\boldsymbol{x}) \cdot \hat{\boldsymbol{J}}(\boldsymbol{x}) \rangle \tag{14.43}$$

be the trial energy functional, where $\boldsymbol{\sigma}$ is the local conductivity tensor. Then among all trial fields $\hat{\boldsymbol{J}}$, the field that makes the associated intensity field irrotational is the one that uniquely minimizes the trial energy functional $W[\hat{\boldsymbol{J}}]$, i.e.,

$$W[\boldsymbol{J}] \leq W[\hat{\boldsymbol{J}}] \qquad \forall \hat{\boldsymbol{J}} \in A_L, \tag{14.44}$$

or, equivalently,

$$\frac{1}{2}\langle \boldsymbol{J} \rangle \cdot \boldsymbol{\sigma}_e^{-1} \cdot \langle \boldsymbol{J} \rangle \leq \frac{1}{2}\langle \hat{\boldsymbol{J}} \cdot \boldsymbol{\sigma}^{-1} \cdot \hat{\boldsymbol{J}} \rangle \qquad \forall \hat{\boldsymbol{J}} \in A_L, \tag{14.45}$$

where $\boldsymbol{J}$ satisfies (14.12).

Proof: Let the "difference" field $\boldsymbol{Q}$ be defined by

$$\boldsymbol{Q} = \hat{\boldsymbol{J}} - \boldsymbol{J} \tag{14.46}$$

such that

$$\nabla \cdot \hat{\boldsymbol{J}} = 0, \quad \langle \hat{\boldsymbol{J}} \rangle = \langle \boldsymbol{J} \rangle.$$

Therefore, $\langle \boldsymbol{Q} \rangle = 0$, and since both $\boldsymbol{J}$ and $\hat{\boldsymbol{J}}$ are solenoidal, $\boldsymbol{Q}$ is also solenoidal, i.e.,

$$\nabla \cdot \boldsymbol{Q} = 0.$$

Consider the identity

$$\langle \hat{\boldsymbol{J}} \cdot \boldsymbol{\sigma}^{-1} \cdot \hat{\boldsymbol{J}} \rangle = \langle \boldsymbol{J} \cdot \boldsymbol{\sigma}^{-1} \cdot \boldsymbol{J} \rangle + 2 \langle \boldsymbol{Q} \cdot \boldsymbol{\sigma}^{-1} \cdot \boldsymbol{J} \rangle + \langle \boldsymbol{Q} \cdot \boldsymbol{\sigma}^{-1} \cdot \boldsymbol{Q} \rangle.$$

Since $\boldsymbol{E} = \boldsymbol{\sigma}^{-1} \cdot \boldsymbol{J} = -\nabla T$, the middle term may be rewritten as

$$\begin{aligned} \langle \boldsymbol{Q} \cdot \boldsymbol{\sigma}^{-1} \cdot \boldsymbol{J} \rangle &= -\langle \boldsymbol{Q} \cdot \nabla T \rangle \\ &= -\lim_{V \to \infty} \frac{1}{V} \int_S T(\boldsymbol{Q} \cdot \boldsymbol{n}) dS + \lim_{V \to \infty} \frac{1}{V} \int_V T(\nabla \cdot \boldsymbol{Q}) dV \\ &= -\lim_{V \to \infty} \frac{1}{V} \int_S T'(\boldsymbol{Q} \cdot \boldsymbol{n}) dS = 0. \end{aligned} \tag{14.47}$$

The second line of (14.47) follows from formula (14.8) with $\boldsymbol{A} = T$ and $\boldsymbol{B} = \boldsymbol{Q}$. The third line results after decomposing T and $\boldsymbol{Q}$ into their mean and fluctuating parts (as in the proof of Theorem 14.1), using the condition $\langle \boldsymbol{Q} \rangle = 0$, and utilizing the fact that $\nabla \cdot \boldsymbol{Q} = 0$. The integral in the third line of (14.47) involving the fluctuating fields is zero by ergodicity. Using this result in combination with energy representation (14.32) gives

$$\langle \hat{\boldsymbol{J}} \cdot \boldsymbol{\sigma}^{-1} \cdot \hat{\boldsymbol{J}} \rangle = \langle \boldsymbol{J} \rangle \cdot \boldsymbol{\sigma}_e^{-1} \cdot \langle \boldsymbol{J} \rangle + \langle \boldsymbol{Q} \cdot \boldsymbol{\sigma}^{-1} \cdot \boldsymbol{Q} \rangle,$$

which proves the statement (14.45). The equality sign holds only when the difference field $\boldsymbol{Q}$ is zero throughout $\mathcal{V}$, i.e., when $\hat{\boldsymbol{J}} = \boldsymbol{J}$. The uniqueness of $\boldsymbol{J}$ follows using the same arguments as for Theorem 14.3. ∎

Remarks:

1. In words, the minimum complementary energy principle states that the actual macroscopic energy $W[\boldsymbol{J}]$ is bounded from above by the trial macroscopic energy $W[\hat{\boldsymbol{J}}]$. Therefore, one can obtain an upper bound on the effective resistivity tensor $\boldsymbol{\sigma}_e^{-1}$ or a lower bound $\boldsymbol{\sigma}_e^L$ on the effective conductivity tensor $\boldsymbol{\sigma}_e$ in the positive semidefinite sense.
2. Theorem 14.4 also applies to periodic media (Bensoussan et al. 1978). Again, boundary terms are over the unit cell and vanish because of periodicity.

$$\lim_{V\to\infty}\frac{1}{V}\int_S \boldsymbol{u}'\boldsymbol{n}dS \to 0; \tag{14.68}$$

i.e., the ratio of the surface integral of (14.68) to the volume V vanishes in the limit $V \to \infty$.

Similarly, for the large region of volume V and surface S, we can express the average of the fluctuating part of the stress as

$$\begin{aligned}\langle\boldsymbol{\tau}'\rangle &\approx \frac{1}{V}\int_V \boldsymbol{\tau}'dV \\ &= \frac{1}{V}\int_V \nabla\cdot(\boldsymbol{x}\boldsymbol{\tau}')dV \\ &= \frac{1}{V}\int_S \boldsymbol{x}(\boldsymbol{\tau}'\cdot\boldsymbol{n})dS.\end{aligned} \tag{14.69}$$

The second line of (14.69) follows from the identity (14.7) with $\boldsymbol{A} = \boldsymbol{x}$ and $\boldsymbol{B} = \boldsymbol{\tau}$ and the fact that $\nabla\cdot\boldsymbol{\tau} = 0$. The third line is obtained from the divergence theorem (14.1) with $\boldsymbol{A}$ equal to the third-order tensor $\boldsymbol{x}\boldsymbol{\tau}'$. Since the traction is continuous across the multiphase interface, the surface integrals over the interface make no contribution in the application of the divergence theorem, and thus we do not bother to write such terms explicitly. Hence, we see from (14.64) and (14.69) that in the infinite-volume limit,

$$\lim_{V\to\infty}\frac{1}{V}\int_S \boldsymbol{x}(\boldsymbol{\tau}'\cdot\boldsymbol{n})dS \to 0. \tag{14.70}$$

To summarize, ergodicity renders the boundary terms involving the fluctuating quantities $\boldsymbol{u}'$ and $\boldsymbol{\tau}'$ in (14.68) and (14.70), respectively, to be zero. In the discussion that follows, boundary terms of these types will arise and will be taken to be zero by ergodicity.

14.2.2 Energy Representation

We recall from Section 13.3.1 that the energy stored per unit volume in a homogeneous linearly elastic material (without body forces) is a positive quantity that is proportional to the double dot product of the strain tensor and the stress tensor (Sokolnikoff 1956). In the case of a heterogeneous linear material, we assume that the scalar energy stored per unit volume $u(\boldsymbol{x})$ at the point $\boldsymbol{x}$ is given by the same but local form, i.e.,

$$u(\boldsymbol{x}) = \frac{1}{2}\boldsymbol{\varepsilon}(\boldsymbol{x}) : \boldsymbol{\tau}(\boldsymbol{x}) \geq 0. \tag{14.71}$$

We will simply refer to u as the "microscopic energy," which should not be confused with the displacement vector $\boldsymbol{u}$. Use of Hooke's law (14.59) shows that the microscopic energy is a nonnegative quadratic form in either the strain or the stress; i.e., one has the equivalent but alternative forms

$$u_{\boldsymbol{\varepsilon}}(\boldsymbol{x}) = \frac{1}{2}\boldsymbol{\varepsilon}(\boldsymbol{x}) : \boldsymbol{C}(\boldsymbol{x}) : \boldsymbol{\varepsilon}(\boldsymbol{x}) \tag{14.72}$$

14.3 Trapping Constant

We will derive variational principles that will enable us to bound the trapping constant γ (or, equivalently, mean survival time τ) from above and below. As in the case of the conduction and elasticity problems, these variational bounds are based on minimizing the "energy" of the system. First, it will be shown that the trapping constant has an energy representation. We then will prove the minimum energy principles that lead to rigorous upper and lower bounds on the trapping constant, or equivalently, the mean survival time.

We will consider *ergodic* porous media with a trap-free, or pore, region $\mathcal{V}_1$ and a trap region $\mathcal{V}_2$. Let the interface between the two regions be denoted by $\partial\mathcal{V}$. Referring to relations (13.148), (13.149), and (13.151), we see that the local equations for the *scaled* concentration field in the instance of perfectly absorbing traps are given by

$$\Delta u = -1 \qquad \text{in } \mathcal{V}_1, \tag{14.115}$$

$$u = 0 \qquad \text{on } \partial\mathcal{V}, \tag{14.116}$$

where we extend u into the trap region $\mathcal{V}_2$ to be zero. The averaged relation that defines the trapping constant γ is

$$\gamma^{-1} = \langle u\, \mathcal{I} \rangle = \langle u \rangle, \tag{14.117}$$

where $\mathcal{I} \equiv \mathcal{I}^{(1)}$ is the indicator function for the trap-free region. The second equality in (14.117) follows from the extension of u into $\mathcal{V}_2$.

14.3.1 Energy Representation

Recall that the trapping constant γ is the proportionality constant in the relation between the average concentration field and production rate per unit volume. We now derive an energy representation for the trapping constant.

Theorem 14.11 *For ergodic media, the trapping constant γ can be rewritten in terms of the energy functional:*

$$\gamma^{-1} = \langle \nabla u(\boldsymbol{x}) \cdot \nabla u(\boldsymbol{x})\, \mathcal{I}(\boldsymbol{x}) \rangle. \tag{14.118}$$

Proof: Let $V_{\mathcal{R}}$ be a very large sphere of radius $\mathcal{R}$ centered at the origin in $\mathcal{V}$, and let $\partial V_{\mathcal{R}}$ be the surface of this sphere. Multiplying the diffusion equation (14.115) by u and ensemble averaging yields

$$\begin{aligned}
\gamma^{-1} &= -\langle u \Delta u \rangle \\
&= -\frac{1}{V_{\mathcal{R}}} \int_{V_{\mathcal{R}}} \langle u \Delta u \rangle dV = -\left\langle \frac{1}{V_{\mathcal{R}}} \int_{V_{\mathcal{R}}} u \Delta u\, dV \right\rangle \\
&= \left\langle \frac{1}{V_{\mathcal{R}}} \int_{V_{\mathcal{R}}} \nabla u \cdot \nabla u dV \right\rangle - \left\langle \frac{1}{V_{\mathcal{R}}} \int_{\partial V_{\mathcal{R}}} u \frac{\partial u}{\partial n} dS \right\rangle - \left\langle \frac{1}{V_{\mathcal{R}}} \int_{\partial \mathcal{V}} u \frac{\partial u}{\partial n} dS \right\rangle
\end{aligned}$$

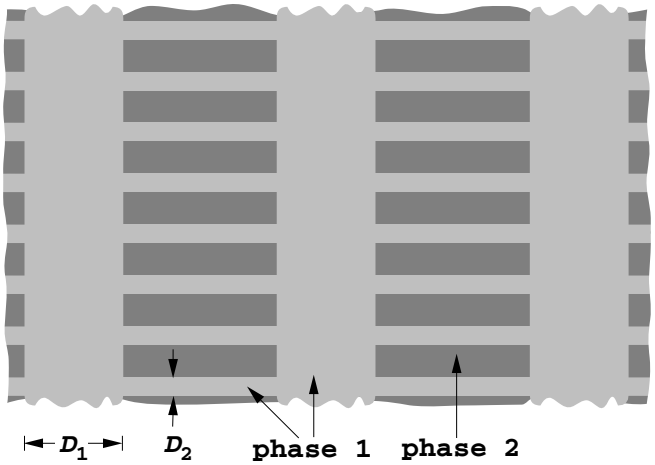

Figure 16.6 An example of a two-dimensional second-rank laminate whose effective conductivity is exactly given by (16.8) in the limit $D_1/D_2 \to \infty$. Here $\boldsymbol{n}^{(1)} \cdot \boldsymbol{n}^{(2)} = 0$.

$$\left(\sigma_e^{(2)}\right)_{11} = \left[\frac{\phi_1^{(2)}}{\sigma_1} + \frac{\phi_2^{(2)}}{\sigma_2}\right]^{-1}, \qquad \left(\sigma_e^{(2)}\right)_{22} = \sigma_1\phi_1^{(2)} + \sigma_2\phi_2^{(2)},$$

where $\phi_i^{(j)}$ is the volume fraction of phase i in the jth stage with $\phi_2 = \phi_2^{(1)}\phi_2^{(2)}$. This result immediately follows from our result (16.10) for the first-rank laminate but for $d = 2$. The effective conductivity tensor of the entire laminate composite is therefore given by

$$\boldsymbol{\sigma}_e = \begin{bmatrix} (\sigma_e)_{11} & 0 \\ 0 & (\sigma_e)_{22} \end{bmatrix}, \tag{16.17}$$

where

$$(\sigma_e)_{11} = \sigma_1\phi_1^{(1)} + (\sigma_e^{(2)})_{11}\phi_2^{(1)}, \qquad (\sigma_e)_{22} = \left[\frac{\phi_1^{(1)}}{\sigma_1} + \frac{\phi_2^{(1)}}{(\sigma_e^{(2)})_{22}}\right]^{-1}.$$

In order for the tensor (16.17) to be isotropic, we must have $(\sigma_e)_{11} = (\sigma_e)_{22}$, implying the volume fraction requirement

$$\phi_1^{(1)} = \frac{\phi_1^{(2)}}{\phi_2^{(2)}}. \tag{16.18}$$

It follows, after some algebra, that the corresponding isotropic effective conductivity is given by

$$\sigma_e = \langle\sigma\rangle - \frac{(\sigma_2 - \sigma_1)^2\phi_1\phi_2}{\langle\tilde{\sigma}\rangle + \sigma_1}, \tag{16.19}$$

where $\langle\sigma\rangle$ and $\langle\tilde{\sigma}\rangle$ are defined by the relations in (16.9). We recognize result (16.19) to be identical to the exact expression for the coated-cylinder model given by (16.8) with

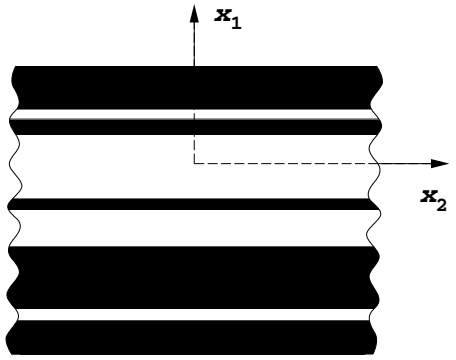

Figure 16.9 Portion of a two-dimensional laminate of rank one.

It is simpler and instructive to consider first the calculation of $\boldsymbol{C}_e$ for the two-dimensional laminate of rank 1 depicted in Figure 16.9. Let E_i and ν_i be the two-dimensional (planar) Young modulus and Poisson ratio of phase i, respectively. The local fields can depend at most upon the x_1 coordinate when uniform fields are imposed at the boundaries. The effective stiffness tensor for this laminate in plane elasticity is most conveniently represented by the 3×3 matrix

$$\boldsymbol{C}_e = \begin{bmatrix} (C_e)_{11} & (C_e)_{12} & 0 \\ (C_e)_{12} & (C_e)_{22} & 0 \\ 0 & 0 & (C_e)_{66} \end{bmatrix}, \tag{16.43}$$

where

$$(C_e)_{11} = \left\langle \frac{1-\nu^2}{E} \right\rangle^{-1}, \quad (C_e)_{12} = \langle \nu \rangle \left\langle \frac{1-\nu^2}{E} \right\rangle^{-1}, \tag{16.44}$$

$$(C_e)_{22} = \langle \nu^2 \rangle \left\langle \frac{1-\nu^2}{E} \right\rangle^{-1} + \langle E \rangle, \qquad (C_e)_{66} = \left\langle G^{-1} \right\rangle^{-1}, \tag{16.45}$$

and for any property c, $\langle c \rangle = c_1\phi_1 + c_2\phi_2$. Since the effective Young moduli in the x_1- and x_2-directions are given by

$$(E_e)_{11} = (C_e)_{11} - \frac{(C_e)_{12}^2}{(C_e)_{22}}, \qquad (E_e)_{22} = (C_e)_{22} - \frac{(C_e)_{12}^2}{(C_e)_{11}},$$

we have that

$$(E_e)_{11} = \left\langle \frac{1-\nu^2}{E} \right\rangle^{-1} \left[\frac{\langle \nu^2 \rangle - \langle \nu \rangle^2 + \langle E \rangle \left\langle \frac{1-\nu^2}{E} \right\rangle}{\langle \nu^2 \rangle + \langle E \rangle \left\langle \frac{1-\nu^2}{E} \right\rangle} \right], \tag{16.46}$$

$$(E_e)_{22} = \langle E \rangle + (\langle \nu^2 \rangle - \langle \nu \rangle^2) \left\langle \frac{1-\nu^2}{E} \right\rangle^{-1}. \tag{16.47}$$

Moreover, since the effective shear modulus $(G_e)_{12}$ is equal to $(C_e)_{66}$, we have that

$$(G_e)_{12} = \langle G^{-1} \rangle^{-1}. \tag{16.48}$$

We see that the effective Young modulus $(E_e)_{22}$ is simply given by the arithmetic average of the phase Young moduli when $\nu_1 = \nu_2$, and the effective shear modulus $(G_e)_{12}$ is given by the harmonic average of the phase shear moduli. Note that it is only when the phase Poisson ratios are equal to zero ($\nu_1 = \nu_2 = 0$), that the effective Young modulus in the x_1-direction, (16.46), reduces to the harmonic average of the Young moduli, i.e.,

$$(E_e)_{11} = \langle E^{-1} \rangle^{-1} . \tag{16.49}$$

We now derive result (16.43). Let us consider applying three independent uniform strain fields: a uniaxial strain ε^0_{11} in the x_1-direction, a uniaxial strain ε^0_{22} in the x_2-direction, and a uniform shear strain ε^0_{12}. The local fields must satisfy the equilibrium equations in each phase, i.e.,

$$\frac{\partial \tau_{11}}{\partial x_1} + \frac{\partial \tau_{12}}{\partial x_2} = 0, \tag{16.50}$$

$$\frac{\partial \tau_{12}}{\partial x_1} + \frac{\partial \tau_{22}}{\partial x_2} = 0, \tag{16.51}$$

and also obey Hooke's law in each phase:

$$\tau_{11}(x_1) = \frac{E(x_1)}{1 - \nu^2(x_1)} \left[\varepsilon_{11}(x_1) + \nu(x_1) \varepsilon_{22}(x_1) \right], \tag{16.52}$$

$$\tau_{22}(x_1) = \frac{E(x_1)}{1 - \nu^2(x_1)} \left[\nu(x_1) \varepsilon_{11}(x_1) + \varepsilon_{22}(x_1) \right], \tag{16.53}$$

$$\tau_{12}(x_1) = 2G(x_1) \varepsilon_{12}(x_{12}). \tag{16.54}$$

Since the local fields are independent of x_2, it follows from (16.50) and (16.51) that $\tau_{11}(x_1)$ and $\tau_{12}(x_1)$ are constants throughout the composite:

$$\tau_{11}(x_1) = \langle \tau_{11} \rangle, \qquad \tau_{12}(x_1) = \langle \tau_{12} \rangle.$$

Moreover, it follows that the local strain in the x_2-direction must be a constant throughout the composite:

$$\varepsilon_{22}(x_1) = \langle \varepsilon_{22} \rangle = \varepsilon^0_{22}.$$

The average of the strain component $\varepsilon_{11}(x_1)$ must satisfy the boundary condition

$$\langle \varepsilon_{11} \rangle = \varepsilon^0_{11}.$$

Therefore, from expression (16.52), we see that the 11-component of strain must be a piecewise constant function according to the relation

$$\varepsilon_{11}(x_1) = \frac{1 - \nu^2(x_1)}{E(x_1)} \langle \tau_{11} \rangle - \nu(x_1) \langle \varepsilon_{22} \rangle. \tag{16.55}$$

Averaging (16.53) [after use of (16.55)], (16.54), and (16.55) yields the averaged constitutive relations

Table 16.1 Coefficients in the low-concentration asymptotic expressions.

Lattice	a_1	a_2	a_3	a_4
SC	−1.396	1.714	2.889	−3.077
BCC	0.430	−0.520	−6.163	3.373
FCC	0.388	−0.411	−5.928	2.750

Notice that result (16.62) for the effective bulk modulus is identical to the exact expression for the coated-cylinder model given by (16.41) with $d = 2$. Unlike the effective shear modulus expression (16.63), the effective bulk modulus expression (16.62) is also exact for a *square symmetric* second-rank laminate, an example of which is depicted in Figure 16.6.

16.2.4 Periodic Arrays of Inclusions

Nunan and Keller (1984) studied the effective moduli of the three cubic arrays of *rigid* spheres in a matrix (phase 1). Such a composite has cubic elastic symmetry, and therefore the effective stiffness tensor is specified by three elastic moduli (see Section 13.3.2) according to the relation

$$(C_e)_{ijkl} = (\lambda_1 + G_1\gamma)\delta_{ij}\delta_{kl} + G_1(1+\beta)(\delta_{ik}\delta_{jl} + \delta_{il}\delta_{jk}) + 2G_1(\alpha - \beta)\delta_{ijkl}. \tag{16.64}$$

This expression corrects a misprint contained in Nunan and Keller (1984). Here $\lambda_1 = K_1 - 2G_1/3$ is the matrix Lamé constant, and δ_{ijkl} is equal to one if all the subscripts are equal and zero otherwise. They found low-density asymptotic relations for the parameters α, β, and γ as follows:

$$\alpha = \frac{15}{2}\frac{(1-\nu_1)\phi_2}{4-5\nu_1}\left[1 - \left(1 - \frac{3a_1}{4-5\nu_1}\right)\phi_2 + \frac{3a_2}{4-5\nu_1}\phi_2^{5/3} + \mathcal{O}\left(\phi_2^{7/3}\right)\right]^{-1},$$

$$\beta = \frac{15}{2}\frac{(1-\nu_1)\phi_2}{4-5\nu_1}\left[1 - \left(1 + \frac{2a_1}{4-5\nu_1}\right)\phi_2 - \frac{2a_2}{4-5\nu_1}\phi_2^{5/3} + \mathcal{O}\left(\phi_2^{7/3}\right)\right]^{-1},$$

$$\gamma = \frac{3(1-\nu_1)\phi_2}{(1-2\nu_1)(4-5\nu_1)}\left[1 - \left(\frac{3\nu_1 + (1-2\nu_1)a_3}{4-5\nu_1}\right)\phi_2 + \frac{(1-2\nu_1)a_4}{4-5\nu_1}\phi_2^{5/3} + \mathcal{O}\left(\phi_2^{7/3}\right)\right]^{-1}.$$

The coefficients a_i in these formulas depend upon the lattice geometry, but not the matrix Poisson ratio ν_1, and are summarized in Table 16.1.

Consider the opposite asymptotic regime of nearly close-packed spheres. The elastic interaction between spheres near the maximum close-packing density is concentrated in the regions near the points of contact, as observed by Flaherty and Keller (1973) and Nunan and Keller (1984). A local analysis of the region between two nearly touching spheres, in conjunction with knowledge of nearest-neighbor locations, produces the dominant contribution of the interaction for the entire sphere.

For cylinders of arbitrary shape, we can write

$$k = \gamma^{-1} = \frac{\phi_1^3}{cs^2}, \tag{16.99}$$

where c is a shape-dependent constant (e.g., $c = 2$ for circles, $c = 5/3$ for equilateral triangles, and $c = 1.78\ldots$ for squares). Equation (16.99) has been applied as an empirical relation for isotropic porous media of arbitrary microstructure; c then is some adjustable parameter ($c = 5$ models many porous media well). This empirical equation has a special status in the literature and is referred to as the *Kozeny–Carman* relation.

The determination of the permeability for flow past dilute arrays of obstacles is treated in Chapter 17.

16.4.2 Periodic Arrays of Obstacles

Hasimoto (1959) obtained low-concentration asymptotic formulas for the fluid permeability k associated with slow viscous flow past spheres of radius R arranged on the sites of the three cubic lattices. Specifically, he found that the dimensionless fluid permeabilities are given by

$$\frac{k}{k_s} = 1 - 1.76011\phi_2^{1/3} + \phi_2 - 1.5593\phi_2^2 + \mathcal{O}\left(\phi_2^{8/3}\right), \qquad \text{(SC)}, \tag{16.100}$$

$$\frac{k}{k_s} = 1 - 1.79186\phi_2^{1/3} + \phi_2 - 0.329\phi_2^2 + \mathcal{O}\left(\phi_2^{8/3}\right), \qquad \text{(BCC)}, \tag{16.101}$$

$$\frac{k}{k_s} = 1 - 1.79175\phi_2^{1/3} + \phi_2 - 0.302\phi_2^2 + \mathcal{O}\left(\phi_2^{8/3}\right), \qquad \text{(FCC)}, \tag{16.102}$$

where $k_s = (2R^2)/(9\phi_2)$ is the Stokes permeability in the infinitely dilute limit (see Chapter 19). The coefficients multiplying $\phi_2^{1/3}$ in the above expressions are identical to those in (16.88) up to the significant figures indicated. Sangani and Acrivos (1982) have obtained asymptotic relations for the fluid permeabilities for all three lattices to very high order in ϕ_2.

Hasimoto also obtained low-concentration asymptotic expressions for the fluid permeability k associated with flow past a square array of circular cylinders of radius R. He found that

$$\frac{k}{k_0} = -\ln\phi_2 - 1.4763 + 2\phi_2 + \mathcal{O}(\phi_2^2), \tag{16.103}$$

where $k_0 = R^2/(8\phi_2)$. For the hexagonal array, Sangani and Acrivos obtained

$$\frac{k}{k_o} = -\ln\phi_2 - 1.4975 + 2\phi_2 + \mathcal{O}(\phi_2^2). \tag{16.104}$$

Sangani and Acrivos (1982) have also found higher-order asymptotic expressions for these two-dimensional lattices.

Table 17.1 Values of the coefficients T_h and T_s defined by (17.102) for the limiting cases of spheres, needles, and disks in three dimensions. For needles, $E_1 \equiv G_1(3K_1 + G_1)/(3K_1 + 7G_1)$, and for disks, $H_2 = G_2(3K_2/2 + 4G_2/3)/(K_2 + 2G_2)$. Corresponding values of N_h and N_s are easily obtained from the formulas (17.101). Note that the results for spheres agree with terms of (17.84) for $d = 3$.

Inclusion Shape	T_h	T_s
Spheres	$\frac{K_1+4G_1/3}{K_2+4G_1/3}$	$\frac{G_1+H_1}{G_2+H_1}$
Needles	$\frac{K_1+G_1+G_2/3}{K_2+G_1+G_2/3}$	$\frac{1}{5}\left[\frac{4G_1}{G_1+G_2} + \frac{2G_1(G_1+E_1)}{(G_2+E_1)} + \frac{K_2+4G_1/3}{K_2+G_1+G_2/3}\right]$
Disks	$\frac{K_1+4G_2/3}{K_2+4G_2/3}$	$\frac{G_1+H_2}{G_2+H_2}$

17.3 Trapping Problem

17.3.1 Spherical Trap

We are interested in obtaining the concentration field exterior to a spherical trap of radius R. This is a classical problem dating back to the work of Smoluchowski (1917). According to the local equation (13.136), the steady-state concentration field satisfies a Poisson equation subject to the appropriate boundary conditions. This system of equations can be replaced by a Laplace equation for the concentration field, with the production term in the Poisson equation replaced by a uniform concentration field at infinity.

Consider inserting a *partially absorbing* three-dimensional spherical trap with radius R and surface rate constant κ into an infinite medium in which the unperturbed concentration field is the uniform value C_0. Let $\boldsymbol{r}$ be the position vector emanating from the trap center (see Figure 17.4). Under steady-state conditions, the local concentration field $c(\boldsymbol{r})$ depends only on the radial distance $r \equiv |\boldsymbol{r}|$ and is governed by

$$\Delta c(\boldsymbol{r}) = \frac{1}{r^2}\frac{\partial}{\partial r}\left(r^2\frac{\partial c}{\partial r}\right) = 0, \qquad r \geq R, \tag{17.103}$$

$$\mathcal{D}\frac{\partial c}{\partial r} = \kappa c, \qquad r = R, \tag{17.104}$$

$$c = C_0, \qquad r \to \infty. \tag{17.105}$$

The general form of the solution of this diffusion equation is given by

$$c(r) = A + \frac{B}{r}, \qquad r \geq R. \tag{17.106}$$

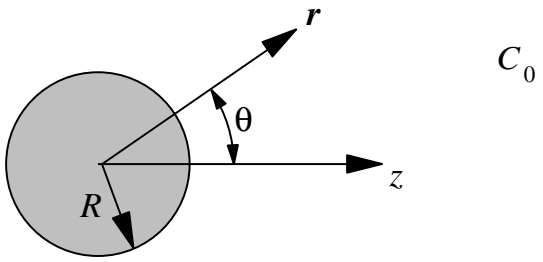

Figure 17.4 Coordinate system for a spherical trap of radius R in an infinite medium with constant concentration field C_0 at infinity.

Application of the boundary conditions reveals that

$$A = C_0, \qquad B = \frac{C_0 \kappa R^2}{\mathcal{D} + \kappa R},$$

and therefore the desired solution is

$$c(r) = C_0 \left[1 + \frac{\kappa R}{\mathcal{D} + \kappa R} \left(\frac{R}{r} \right) \right], \qquad r \geq R. \tag{17.107}$$

The total flux J_T into the sphere can be calculated by integrating the normal flux over the surface of the sphere, i.e.,

$$\begin{aligned} J_T &= \int_{r=R} -\mathcal{D} \, \nabla c \cdot \boldsymbol{n} \, R^2 d\Omega \\ &= \frac{4\pi \, \kappa R^2 \mathcal{D} C_0}{\kappa R + \mathcal{D}}, \end{aligned} \tag{17.108}$$

where $d\Omega$ is the differential solid angle contained in a three-dimensional sphere.

In the *diffusion-controlled* case ($\kappa R/\mathcal{D} = \infty$), the solution (17.107) gives

$$c(r) = C_0 \left[1 - \left(\frac{R}{r} \right) \right], \qquad r \geq R, \tag{17.109}$$

and the total flux (17.108) becomes

$$J_T = 4\pi R \mathcal{D} C_0. \tag{17.110}$$

Of course, in the *reaction-controlled* case ($\kappa R/\mathcal{D} = 0$), the solution (17.107) is trivial, i.e., $c = C_0$ and $J_T = 0$, since there is no absorption.

The solution of the concentration field obtained above for a spherical trap in three dimensions has no analogue in two dimensions. Specifically, there is no solution of the Laplace equation for a circular trap in an infinite medium with an unperturbed concentration field C_0 that simultaneously satisfies the condition $c = 0$ on the trap surface and the boundary condition at infinity. The nonexistence of such a solution is the analogue of Stokes's paradox, described in the next section in the case of uniform flow past a circular disk.

The concentration field for a d-dimensional spherical trap of radius R for any $d \geq 3$ can be obtained from the boundary value problem

$$\frac{1}{r^{d-1}}\frac{\partial}{\partial r}\left(r^{d-1}\frac{\partial c}{\partial r}\right) = 0, \qquad r \geq R, \tag{17.111}$$

$$\mathcal{D}\frac{\partial c}{\partial r} = \kappa c, \qquad r = R, \tag{17.112}$$

$$c = C_0, \qquad r \to \infty. \tag{17.113}$$

The solution of this boundary value problem is

$$c(r) = C_0\left[1 + \frac{\kappa R}{(d-2)\mathcal{D} + \kappa R}\left(\frac{R}{r}\right)^{d-2}\right], \qquad r \geq R. \tag{17.114}$$

The total flux J_T into the sphere is then

$$\begin{aligned} J_T &= \int_{r=R} -\mathcal{D}\,\nabla c \cdot \boldsymbol{n}\, R^{d-1} d\Omega \\ &= \frac{(d-2)\Omega\,\kappa R^{d-1}\mathcal{D}C_0}{\kappa R + (d-2)\mathcal{D}}, \qquad d \geq 3 \end{aligned} \tag{17.115}$$

where $\Omega(d)$ is the total solid angle contained in a d-dimensional sphere, given by (2.56).

In the *diffusion-controlled* case ($\kappa R/\mathcal{D} = \infty$), the solution (17.114) becomes

$$c(r) = C_0\left[1 - \left(\frac{R}{r}\right)^{d-2}\right], \qquad r \geq R. \tag{17.116}$$

From (17.115), we find that the total flux in this instance becomes

$$J_T = (d-2)\Omega\, R^{d-2}\mathcal{D}C_0. \tag{17.117}$$

17.3.2 Spheroidal Trap

Consider a perfectly absorbing spheroidal trap in three dimensions with semiaxes $a_1 = a_2 = a$ and $a_3 = b$ in which the concentration at infinity is C_0. The concentration field c outside of this trap is obtained by solving $\Delta c = 0$ in spheroidal coordinates (η, θ, ψ) (Abramowitz and Stegun 1972), with $c(\mathcal{S}) = 0$ on the trap surface $\mathcal{S}$ and $c = C_0$ at infinity (Miller, Kim and Torquato 1991). The level surfaces of η (η = constant) are a confocal family of spheroids having their common center at the origin. The trap surface $\mathcal{S}$, defined by $\eta = \eta_0$, is related to the semiaxes a and b through

$$a = \sqrt{b^2 - a^2}\sinh\eta_0, \qquad b = \sqrt{b^2 - a^2}\cosh\eta_0, \qquad b \geq a, \tag{17.118}$$

$$a = \sqrt{a^2 - b^2}\cosh\eta_0, \qquad b = \sqrt{a^2 - b^2}\sinh\eta_0, \qquad b \leq a. \tag{17.119}$$

The coordinates θ and ψ are angles.

By symmetry, c is a function only of η and in prolate spheroidal coordinates (Miller et al. 1991) the governing equations simplify as follows:

We also discuss the behavior of the effective conductivity of isotropic media as d tends to infinity.

20.1.1 Integral Equation for Cavity Electric Field

Consider a *large* but finite-sized ellipsoidal macroscopically anisotropic composite specimen in arbitrary space dimension d composed of two isotropic phases with conductivities σ_1 and σ_2. The shape of the composite specimen is purposely chosen to be nonspherical, since any rigorously correct expression for the effective conductivity tensor must ultimately be independent of the shape of the composite specimen in the infinite-volume limit. The microstructure is perfectly general and possesses a characteristic microscopic length scale that is much smaller than the semiaxes of the ellipsoid. Thus, the specimen is virtually statistically homogeneous. Ultimately, we will take the infinite-volume limit and hence consider statistically homogeneous media. The local scalar conductivity $\sigma(\boldsymbol{x})$ is expressible as

$$\sigma(\boldsymbol{x}) = \sigma_1 \mathcal{I}^{(1)}(\boldsymbol{x}) + \sigma_2 \mathcal{I}^{(2)}(\boldsymbol{x}), \tag{20.2}$$

where

$$\mathcal{I}^{(p)}(\boldsymbol{x}) = \begin{cases} 1, & \boldsymbol{x} \text{ in phase } p, \\ 0, & \text{otherwise}, \end{cases} \tag{20.3}$$

is the indicator function for phase p ($p = 1, 2$).

Now let us embed this d-dimensional ellipsoidal composite specimen in an infinite *reference* phase q, which is subjected to an applied electric field $\boldsymbol{E}_0(\boldsymbol{x})$ at infinity (see Figure 20.1). The reference phase can be chosen to be arbitrary, but for our purposes, we will take it to be either phase 1 or phase 2, i.e., $q = 1$ or $q = 2$. Introducing the *polarization* field defined by

$$\boldsymbol{P}(\boldsymbol{x}) = [\sigma(\boldsymbol{x}) - \sigma_q]\boldsymbol{E}(\boldsymbol{x}) \tag{20.4}$$

enables us to reexpress the flux $\boldsymbol{J}$, defined by Ohm's law (13.6), as follows:

$$\boldsymbol{J}(\boldsymbol{x}) = \sigma_q \boldsymbol{E}(\boldsymbol{x}) + \boldsymbol{P}(\boldsymbol{x}). \tag{20.5}$$

The vector $\boldsymbol{P}(\boldsymbol{x})$ is the *induced flux polarization field* relative to the medium in the absence of phase p and hence is zero in the reference phase q and nonzero in the "polarized" phase p ($p \neq q$). Throughout the chapter, the indices p and q will be reserved only for the polarized and reference phases, respectively. The choice of which is the reference or polarized phase is arbitrary; all of the results are valid for any $p \neq q$, i.e., $p = 1$ and $q = 2$ or $p = 2$ and $q = 1$.

Under steady-state conditions without sources, the flux is divergence-free [cf. (13.3)], and hence, with the aid of (20.5), this solenoidal condition can be rewritten as

$$\sigma_q \Delta \hat{\varphi}(\boldsymbol{x}) = \nabla \cdot \boldsymbol{P}(\boldsymbol{x}), \tag{20.6}$$

$$H^{(q)}_{ijkl}(\boldsymbol{r}) = \frac{1}{2\Omega[dK_q + 2(d-1)G_q]}\frac{1}{r^d}\Big[\alpha_q\delta_{ij}\delta_{kl} - d(\delta_{ik}\delta_{jl} + \delta_{il}\delta_{jk}) - d\alpha_q(\delta_{ij}n_kn_l + \delta_{kl}n_in_j) + \frac{d(d-\alpha_q)}{2}(\delta_{ik}n_jn_l + \delta_{il}n_jn_k + \delta_{jk}n_in_l + \delta_{jl}n_in_k) + d(d+2)\alpha_q n_in_jn_kn_l\Big], \quad (20.102)$$

where

$$\alpha_q = dK_q/G_q + (d-2) \quad (20.103)$$

is a dimensionless parameter. It is understood that integrals involving the fourth-order tensor $\boldsymbol{H}^{(q)}$ are to be carried out by excluding at $\boldsymbol{x}' = \boldsymbol{x}$ an infinitesimal sphere in the limit that the sphere radius shrinks to zero. The tensor $H^{(q)}_{ijkl}$ is symmetric with respect to the first two indices, to the second two indices, and to interchange of ij and kl, i.e.,

$$H^{(q)}_{ijkl} = H^{(q)}_{jikl} = H^{(q)}_{ijlk} = H^{(q)}_{klij}.$$

Moreover, the integral of $\boldsymbol{H}^{(q)}(\boldsymbol{r})$ over the surface of a sphere of radius $R > 0$ is identically zero, i.e.,

$$\int_{r=R} \boldsymbol{H}^{(q)}(\boldsymbol{r})d\Omega = 0. \quad (20.104)$$

Some contractions of the tensor $\boldsymbol{H}^{(q)}$ that will be of use to us in the subsequent analysis are as follows:

$$H^{(q)}_{ijkk}(\boldsymbol{r}) = \frac{d}{\Omega[dK_q + 2(d-1)G_q]}\frac{1}{r^d}(dn_in_j - \delta_{ij}), \quad (20.105)$$

$$H^{(q)}_{iikl}(\boldsymbol{r}) = \frac{d}{\Omega[dK_q + 2(d-1)G_q]}\frac{1}{r^d}(dn_kn_l - \delta_{kl}), \quad (20.106)$$

$$H^{(q)}_{iikk}(\boldsymbol{r}) = H^{(q)}_{ikik}(\boldsymbol{r}) = 0. \quad (20.107)$$

We will also utilize the following scalar identities:

$$H^{(q)}_{iikl}(\boldsymbol{r})H^{(q)}_{kljj}(\boldsymbol{s}) = \frac{d^3}{\Omega^2[dK_q + 2(d-1)G_q]^2}\frac{1}{r^d}\frac{1}{s^d}[d(\boldsymbol{n}\cdot\boldsymbol{m})^2 - 1], \quad (20.108)$$

$$H^{(q)}_{ijkl}(\boldsymbol{r})H^{(q)}_{klij}(\boldsymbol{s}) = \frac{1}{4\Omega^2[dK_q + 2(d-1)G_q]^2}\frac{1}{r^d}\frac{1}{s^d}\Big\{d(d+2)\alpha_q^2[d(d+2)(\boldsymbol{n}\cdot\boldsymbol{m})^4 - 3] - d(5d+6)\alpha_q^2[d(\boldsymbol{n}\cdot\boldsymbol{m})^2 - 1] + 2d^2(d-2)\alpha_q[d(\boldsymbol{n}\cdot\boldsymbol{m})^2 - 1] + d^3(d+2)[d(\boldsymbol{n}\cdot\boldsymbol{m})^2 - 1]\Big\}, \quad (20.109)$$

where $\boldsymbol{m} = \boldsymbol{s}/|\boldsymbol{s}|$ is a unit vector in the direction of $\boldsymbol{s}$.

At this stage of the analysis, Torquato (1997) departed from previous treatments by introducing an integral equation for the "cavity" strain field $\boldsymbol{f}$. Specifically, upon substitution of (20.100) into expression (20.99), we obtain the integral equation

$$\boldsymbol{f}(\boldsymbol{x}) = \boldsymbol{\varepsilon}_0(\boldsymbol{x}) + \int_\epsilon d\boldsymbol{x}'\boldsymbol{H}^{(q)}(\boldsymbol{x} - \boldsymbol{x}') : \boldsymbol{p}(\boldsymbol{x}), \quad (20.110)$$

onal polynomials. As in the case of the microstructural parameters M_1 and M_2, the three-point parameters N_1 and N_2 are not independent of one another; specifically, one has that

$$N_1 + N_2 = (d-1)\phi_1\phi_2. \tag{20.167}$$

This is shown using the fact that relation (20.163) yields the effective shear modulus G_e exactly through third order in the difference in the moduli and that G_e remains invariant under different labeling of the reference phase.

For any space dimension d, Torquato (1997) has shown that N_p is related to a parameter η_p that lies in the interval $[0, 1]$ via the relation

$$\begin{aligned}\eta_p &= \frac{N_p}{(d-1)\phi_1\phi_2} \\ &= -\frac{(d+2)(5d+6)}{d^2}\zeta_p + \frac{(d+2)^2}{(d-1)\phi_1\phi_2}J[\bar{S}_3^{(p)}],\end{aligned} \tag{20.168}$$

where ζ_p is given by (20.63). Thus, combining (20.167) and (20.168) gives

$$\eta_1 + \eta_2 = 1. \tag{20.169}$$

As in the case of ζ_p, the d^2-fold integral of the operator (20.166) can be reduced (by integrating over angles) to a threefold integral over the lengths r, s, and t of the sides of the triangle or, equivalently, over the two lengths r and s and the angle θ opposite the side of length t, where $t^2 = r^2 + s^2 - 2rs\cos\theta$, with $\cos\theta = \boldsymbol{n}\cdot\boldsymbol{m}$. For $d = 2$, we recover the result

$$\eta_p = \frac{16}{\pi\phi_q\phi_p}\int_0^\infty \frac{dr}{r}\int_0^\infty \frac{ds}{s}\int_0^\pi d\theta\cos(4\theta)\left[S_3^{(p)}(r,s,t) - \frac{S_2^{(p)}(r)S_2^{(p)}(s)}{\phi_p}\right], \tag{20.170}$$

first given by Milton (1982), and for $d = 3$, we recover the result

$$\eta_p = \frac{5\zeta_p}{21} + \frac{150}{7\phi_q\phi_p}\int_0^\infty \frac{dr}{r}\int_0^\infty \frac{ds}{s}\int_{-1}^1 d(\cos\theta)P_4(\cos\theta)\left[S_3^{(p)}(r,s,t) - \frac{S_2^{(p)}(r)S_2^{(p)}(s)}{\phi_p}\right], \tag{20.171}$$

first given by Milton (1981b). Here P_4 is the Legendre polynomial of order four.

As in the case of the operator (20.64) that defines ζ_2, the operator (20.166) has two simple properties: (i) If the function f does not depend on t, then

$$J[f(r,s)] = 0 \tag{20.172}$$

by virtue of the orthogonality of the spherical harmonics; (ii) less obviously, if f depends only on t, then

$$J[f(t)] = \frac{2(3d^2+8d+6)}{d^2}[f(0) - f(\infty)], \tag{20.173}$$

Substitution of this last inequality into the three-point upper bound (21.40), under the condition that $\boldsymbol{\sigma}_2 \geq \boldsymbol{\sigma}_1$, yields the two-point upper bound (21.26). The corresponding two-point lower bound can be obtained from the three-point lower bound in the same fashion.

Using an elegant continued-fractions formalism, Milton (1987) derived formal n-point bounds that, for $n = 3$, are equivalent to the Sen–Torquato anisotropic bounds. The bounds are formal in that the microstructural parameters are not explicitly given in terms of the n-point probability functions. However, important tensor properties of the parameters follow readily from this treatment, which is not the case using the approach of Sen and Torquato.

Four-Point Bounds

Four-point bounds on the effective conductivity can be derived using the aforementioned procedures. We will not derive such bounds here but will instead state four-point bounds for isotropic media. Milton (1981a) was the first to derive such bounds. Sen and Torquato (1989) found anisotropic analogues of these bounds, which in the isotropic case and for $\sigma_2 \geq \sigma_1$ reduce to the following form:

$$\sigma_L^{(4)} \leq \sigma_e \leq \sigma_U^{(4)}, \tag{21.42}$$

where

$$\frac{\sigma_L^{(4)}}{\sigma_1} = \frac{1 + [(d-1)\phi_2 - \gamma_2/\zeta_2]\beta_{21} + (1-d)[\phi_1\zeta_2 + \phi_2\gamma_2/\zeta_2]\beta_{21}^2}{1 - [\phi_2 + \gamma_2/\zeta_2]\beta_{21} + [\phi_1(1-d)\zeta_2 + \phi_2\gamma_2/\zeta_2]\beta_{21}^2}, \tag{21.43}$$

$$\frac{\sigma_U^{(4)}}{\sigma_2} = \frac{1 + [(d-1)\phi_1 - \gamma_1/\zeta_1]\beta_{12} + (1-d)[\phi_2\zeta_1 + \phi_1\gamma_1/\zeta_1]\beta_{12}^2}{1 - [\phi_1 + \gamma_1/\zeta_1]\beta_{12} + [\phi_2(1-d)\zeta_1 + \phi_1\gamma_1/\zeta_1]\beta_{12}^2}, \tag{21.44}$$

$$\gamma_1 - \gamma_2 = (d-2)(\zeta_2 - \zeta_1), \tag{21.45}$$

and

$$\beta_{ij} = \frac{\sigma_i - \sigma_j}{\sigma_i + (d-1)\sigma_j}, \qquad i \neq j. \tag{21.46}$$

The four-point bounds (21.42) depend upon ϕ_i, ζ_i, and the four-point parameters γ_i [defined by (20.60) and related to $\boldsymbol{a}_4^{(i)}$ of (20.52)], which depend upon $S_1^{(i)}$, $S_2^{(i)}$, $S_3^{(i)}$, and $S_4^{(i)}$. Note that for $d = 2$, the four-point parameters are exactly zero ($\gamma_1 = \gamma_2 = 0$), and hence the four-point bounds depend only on the phase volume fractions and parameter $\zeta_2 = 1 - \zeta_1$.

For $d = 2$, Milton (1981a) showed that the four-point bounds (21.42) are realized by space-filling doubly-coated cylinders (circular disks in two dimensions). Each cylinder (disk) is similar, within a scale factor, to any other multicoated cylinder in the composite, and there is a distribution in their sizes ranging to the infinitesimally small (see Figure 21.1). Note that when the radius of the inner cylinder goes to zero, i.e., $\zeta_i \to 0$ ($i = 1, 2$), one recovers the singly coated cylinder assemblages corresponding to the Hashin–Shtrikman two-point bounds.

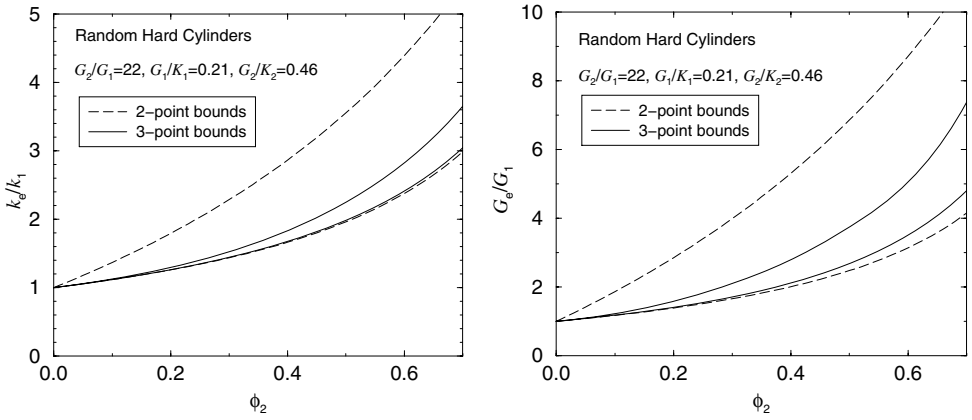

Figure 22.12 Bounds on the scaled effective transverse elastic moduli for a glass–epoxy composite composed of aligned infinitely long nonoverlapping identical circular cylindrical fibers in equilibrium versus fiber volume fraction ϕ_2. Left panel: Bulk modulus from (22.30). Right panel: Shear modulus from (22.55).

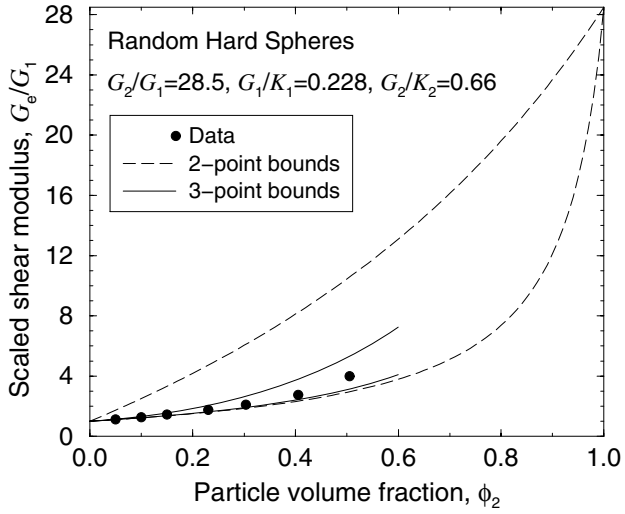

Figure 22.13 Bounds on G_e/G_1 versus ϕ_2 for random equilibrium arrays of identical glass spheres ($d = 3$) in an epoxy matrix. Experimental data are from Smith (1976).

modulus K_e for this model. Included in the figure is the prediction of the three-point approximation (20.184), which, for reasons given in Section 20.2.5, is expected to provide a fairly accurate estimate of K_e. The bounds are qualitatively similar to the corresponding conductivity bounds for perfectly insulating overlapping spheres (see Figure 22.7)

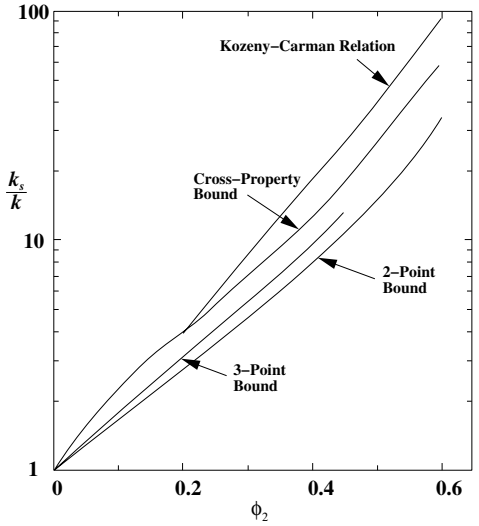

Figure 22.18 Comparison of bounds on the scaled inverse fluid permeability (resistance) k_s/k for equilibrium arrays of identical three-dimensional nonoverlapping spheres of radius R versus sphere volume fraction ϕ_2. Included is two-point interfacial-surface lower bound (21.140), optimized three-point cluster lower bound described below, cross-property bound (23.50), and empirical Kozeny-Carman relation (16.99) with $c = 5$. Here $k_s = 2R^2/(9\phi_2)$.

Figure 22.18 compares, for equilibrium nonoverlapping spheres, the lower bound on k, or equivalently, upper bound on the inverse fluid permeability (resistance) k^{-1}, obtained from (21.140), to the *optimized* three-point cluster lower bound described in Section 22.4.3 and the cross-property bound (23.50) that utilizes information about the mean survival time. Included in the figure is the *empirical* Kozeny-Carman relation (16.99) with $c = 5$. It is seen that the three-point bound is superior to the two-point bound. However, the cross-property bound is the sharpest.

The two-point interfacial-surface upper bound (21.140) also has been computed for dilute concentrations of identical spheres of radius R in the equilibrium cherry-pit model (Torquato and Beasley 1987). This upper bound, for $d = 3$, becomes the following lower bound on the resistance k^{-1}:

$$\frac{k_s}{k} \geq 1 + \left(\frac{15}{8} + \frac{25}{8}\lambda\right)\phi_2 + \mathcal{O}(\phi_2^2). \tag{22.82}$$

Note that this result for the scaled resistance is identical to (22.62) for the scaled trapping constant. Again, as before, the effect of increasing the impenetrability index λ is to increase the scaled resistance.

The interfacial-surface bound has been computed for overlapping spherical grains with a continuous size distribution (Torquato and Lu 1990). These results are summarized in Figure 22.19, where the scaled resistance k_s/k is plotted versus ϕ_2 for the Schulz distribution (6.5). The generalized dilute Stokes result for polydisperse spheres

This class includes packed beds of particles, soils, and sandstones. They showed that bound (23.69) can be violated for porous media containing many isolated pores and dead-end regions whose sizes are on the order of or smaller than the exact effective length scale L appearing in (23.51). Relation (23.69) cannot be generally true, since from Theorem 13.3, $T_1 \geq \tau$.

4. There are two noteworthy approximate cross-property relations linking the permeability k to diffusion parameters. Johnson, Koplik and Schwartz (1986) obtained the following very useful three-dimensional approximation:

$$k \approx \frac{\Lambda^2}{8F}, \tag{23.70}$$

where Λ^2 is a dynamically weighted ratio of V_1/S (pore volume to surface area) involving the electric field, i.e.,

$$\frac{2}{\Lambda} = \frac{\int_{\mathcal{S}} |\boldsymbol{E}(\boldsymbol{x})|^2 dS}{\int_{\mathcal{V}_1} |\boldsymbol{E}(\boldsymbol{x})|^2 dV}. \tag{23.71}$$

Here $\mathcal{S}$ and $\mathcal{V}_1$ denote the pore–solid interface and pore phase, respectively. The formula (23.70) provides a good estimate of k for a variety of porous media and is usually superior to the well-known Kozeny–Carman relation (16.99), which just involves the simple length scale V_1/S. Schwartz, Martys, Bentz, Garboczi and Torquato (1993) found that the relation

$$k \approx \frac{\phi_1 \mathcal{D} \tau}{F} \tag{23.72}$$

gives accurate estimates of the permeabilities of realistic models of porous media. Coker et al. (1996) showed that it also provides a good estimate of the permeability of a Fontainebleau sandstone. Note that relation (23.72) is obtained by multiplying the right-hand side of (23.69) by ϕ_1.

23.2.3 Viscous and Diffusion Relaxation Times

Using a classical Rayleigh–Ritz variational principle, Avellaneda and Torquato (1991) proved that the principal viscous and diffusion relaxation times obey the inequality stated immediately below.

Theorem 23.9 *For any porous medium, the following inequality holds between* Θ_1 *and* T_1*:*

$$\nu \Theta_1 \leq \mathcal{D} T_1. \tag{23.73}$$

Thus, a measurement of the viscous relaxation time Θ_1 (inversely proportional to the smallest eigenvalue of the Stokes operator) can be used to determine information about the diffusion relaxation time T_1, and vice versa. The relaxation time T_1 can be